UNIVERSITY OF CALIFORNIA
RIVERSIDE

Van der Waals Heterostructure Devices: From Monolayer Graphene to Twisted Bilayer Graphene

A Dissertation submitted in partial satisfaction
of the requirements for the degree of

Doctor of Philosophy

in

Physics

by

Rui Lv

June 2019

Dissertation Committee:

Dr. Marc W. Bockrath, Co-Chairperson
Dr. Peng Wei, Co-Chairperson
Dr. Roger Lake

The Dissertation of Rui Lv is approved:

Committee Co-Chairperson

Committee Co-Chairperson

University of California, Riverside

Acknowledgment

First and foremost, I would like to thank my advisor Prof. Marc Bockrath. It has been a great time to study and work in Prof. Marc Bockrath's lab in the past five years. I really feel grareful to have a kind, patient and insightful mentor like him in my PhD career.

I would also like to thank the committee members of my candidacy exams: Prof. Peng Wei, Prof. Roger Lake, Prof. Jory Yarmoff, Prof. Ward Beyermann, and Prof. Jianlin Liu. And I would like to thank Prof. Jeanie Lau for the collaborations and inspiring discussions.

It is impossible to complete this dissertation without the efforts from former and current members in my lab, including Tengfei Miao, Juan Aguilera Servin, Oleg Martynov, Peng Wang, Bin Cheng, Cheng Pan, Yong Wu, Yi Wu, Sean Nelson, Adrian Nosek, Zachary Tuchfeld, Nicholas Mazzucca, Dongying Wang, and Devin Ryan. I enjoy the time working with them and I would like to thank them for countless valuable discussions over the past years.

The support from family gives me the courage to move on no matter how many difficulties I must face in life and study. I would like to thank my parents for their unconditional love. And I would like to thank my wife, Yuning Shen, for the company both physically and spiritually.

In memory of my grandmother

ABSTRACT OF THE DISSERTATION

Van der Waals Heterostructure Devices: From Monolayer Graphene to Twisted Bilayer Graphene

by

Rui Lv

Doctor of Philosophy, Graduate Program in Physics
University of California, Riverside, June 2019
Dr. Marc W. Bockrath, Co-Chairperson
Dr. Peng Wei, Co-Chairperson

In this dissertation, I report my work on making two-dimensional van der Waals heterostructure devices. Chapter one introduces the main concepts of the band structure of graphene and the quantum Hall effect. These are the necessary theoretical foundation to understand transport experiment results in the following chapters. Chapter two includes the device fabrication techniques and recipes for fabrication. In Chapter three, I illustrate different characterization methods to study the properties of van der Waals heterostructure devices. Chapter four presents more detailed work on transport measurements of twisted bilayer graphene devices.

Contents

List of figures

List of Tables

Chapter 1 Introduction

1.1 Basic Concepts in Graphene

1.1.1 lattice and band structure of graphene

Graphene is a single layer of carbon atoms arranged in the two-dimensional (2D) honeycomb lattice. It can be considered as the building block of its allotropes such as graphite, carbon nanotube, and fullerenes [1]. The crystal structure of graphene is shown in Fig 1-1. There are two carbon atoms per unit cell, labeled as A, B. Each A(B) carbon bonds to three B(A) carbons as its nearest neighbors. The primitive vectors for the Bravais lattice are:

$$\vec{a} = a_0\left(-\frac{1}{2}, -\frac{\sqrt{3}}{2}\right) \text{ and } \vec{b} = a_0\left(-\frac{1}{2}, \frac{\sqrt{3}}{2}\right) \quad (1\text{-}1)$$

and the primitive vectors for reciprocal lattice are:

$$\vec{a}^* = \frac{2\pi}{a_0}\left(-1, -\frac{1}{\sqrt{3}}\right) \text{ and } \vec{b}^* = \frac{2\pi}{a_0}\left(-1, \frac{1}{\sqrt{3}}\right) \quad (1\text{-}2)$$

here $a_0 = 0.246$ nm is the lattice constant. High symmetry points Γ, M, K and K' in the Brillouin zone (BZ) are also shown in Fig 1.1

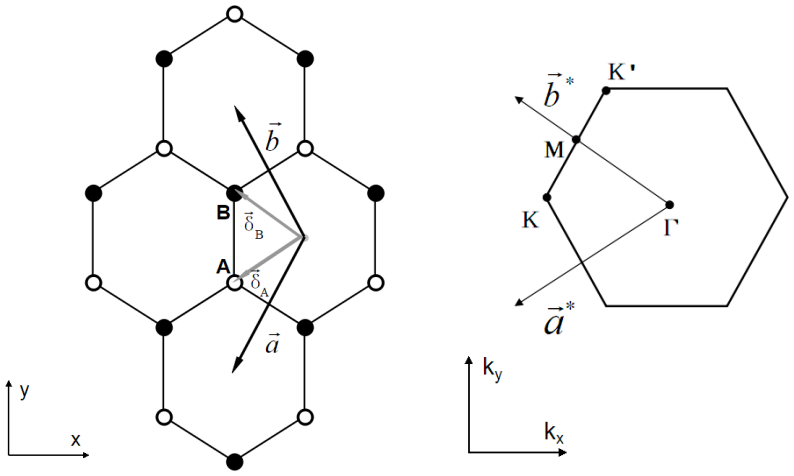

Fig 1-1 Lattice structure of graphene in real space and k-space.

The outer configuration of carbon atom has four electrons. In the honeycomb lattice, 2s, $2p_x$ and $2p_y$ orbits hybridized to form σ bonds between atoms, while the $2p_z$ orbits form the delocalized π bonds. Most of the electronic transport properties in graphene can be understand in terms of the $2p_z$ orbit. Using a simple nearest neighbor tight-binding method on this p_z orbit, the band structure of graphene can be well described [2]

In light of the tight-binding method, we write the solution to the full crystal Schrodinger equation as:

$$\psi(\mathbf{r};\mathbf{k}) = \sum_{\mathbf{R}} e^{i\,\mathbf{k}\cdot\mathbf{R}}\,\varphi(\mathbf{r}-\mathbf{R}) \qquad (1\text{-}3)$$

where

$$\varphi(\mathbf{r}) = c_A\, \psi_z(\mathbf{r}+\boldsymbol{\delta}_A) + c_B\, \psi_z(\mathbf{r}+\boldsymbol{\delta}_B) \tag{1-4}$$

Multiply the crystal Schrodinger equation

$$(\widehat{H}_{at} + \widehat{\Delta V}(\mathbf{r}))\, \psi(\mathbf{r};\mathbf{k}) = E_{\mathbf{k}}\, \psi(\mathbf{r};\mathbf{k}) \tag{1-5}$$

by $\psi_z{}^*(\mathbf{r}+\boldsymbol{\delta}_A)$ and $\psi_z{}^*(\mathbf{r}+\boldsymbol{\delta}_B)$, we will get an eigenvalue equation that determines c_A and c_B.(In the above equations, ψ_z is the atomic wave function for $2p_z$ orbit; $\boldsymbol{\delta}_A$ and $\boldsymbol{\delta}_B$ as shown in Fig 1.1, $\widehat{H}_{at}$ is the atomic Hamiltonian for atoms in the primitive cell located at the origin and $\widehat{\Delta V}(\mathbf{r})$ contains all the corrections to produce the full crystal potential.)

If we include only the nearest neighbors in the eigenvalue equation, the solution is in a simple form:

$$\begin{pmatrix} E_{\mathbf{k}} - E_0 & \gamma_0\, f(\mathbf{k}) \\ \gamma_0\, f^*(\mathbf{k}) & E_{\mathbf{k}} - E_0 \end{pmatrix} \begin{pmatrix} c_A \\ c_B \end{pmatrix} = 0 \tag{1-6}$$

with

$$E_0 = E_p + \int d\mathbf{r}\ \ \psi_z{}^*(\mathbf{r}+\boldsymbol{\delta}_A)\widehat{\Delta V}(\mathbf{r})\, \psi_z(\mathbf{r}+\boldsymbol{\delta}_A) \tag{1-7a}$$

$$\gamma_0 = -\int d\mathbf{r}\ \ \psi_z{}^*(\mathbf{r}+\boldsymbol{\delta}_A)\widehat{\Delta V}(\mathbf{r})\, \psi_z(\mathbf{r}+\boldsymbol{\delta}_B) \tag{1-7b}$$

$$f(\mathbf{k}) = 1 + e^{-i\,\mathbf{k}\cdot\vec{\mathrm{a}}} + e^{i\,\mathbf{k}\cdot\vec{\mathrm{b}}} \tag{1-7c}$$

the eigenvalues are given by,

$$\det(E_{\boldsymbol{k}} - H) = \begin{vmatrix} E_{\mathbf{k}} - E_0 & \gamma_0\, f(\mathbf{k}) \\ \gamma_0\, f^*(\mathbf{k}) & E_{\mathbf{k}} - E_0 \end{vmatrix} = 0 \tag{1-8}$$

that is:

$$\mathrm{E}_k = E_0 \pm \gamma_0 \sqrt{3 + 2\,\mathrm{Cos}(\mathbf{k}\cdot\vec{\mathrm{a}}) + 2\,\mathrm{Cos}(\mathbf{k}\cdot\vec{\mathrm{b}}) + 2\mathrm{Cos}(\mathbf{k}\cdot(\vec{\mathrm{a}}+\vec{\mathrm{b}}))} \tag{1-9}$$

$\gamma_0$is also known as the hopping energy, which is related to the intralayer hopping of the nearest neighbor and the experimental value is ~ 3eV [1]. A 3D plot of the energy band is shown in Fig 1-2

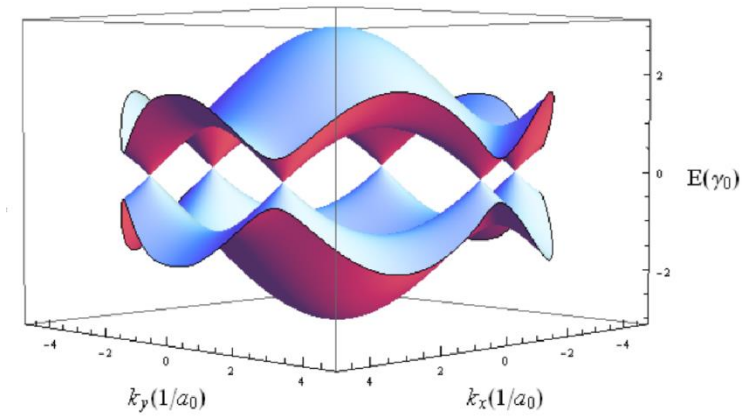

Fig 1-2 3D plot of energy dispersion relation of graphene in k-space.

1.1.2 Dirac fermions

Taking a close look at the energy band in Fig 1.2, we can see the gap is exactly zero at K and K'. Furthermore, the energy shows a linear dependence on **|k|** [3]. To check this, let's go back to equation (1-9) and let E_0 to be the "zero energy" and expand **k** at K, that is,

$$\mathbf{k} = \frac{1}{3}(\vec{\mathbf{a}}^* + \vec{\mathbf{b}}^*) + \Delta\mathbf{k} \tag{1-10}$$

then $f(\mathbf{k}) = 1 + e^{-i\,(\frac{2\pi}{3}+\Delta\mathbf{k}\cdot\vec{\mathbf{a}})} + e^{i\,(\frac{2\pi}{3}+\Delta\mathbf{k}\cdot\vec{\mathbf{b}})}$ and the Hamiltonian becomes,

$$\mathrm{H} = \frac{\sqrt{3}}{2}\gamma_0 \mathrm{a}_0 \begin{pmatrix} 0 & \Delta k_x - i\,\Delta k_y \\ \Delta k_x + i\,\Delta k_y & 0 \end{pmatrix} + O(k^2) \approx \hbar \mathrm{v}_F \vec{\sigma}\cdot\overrightarrow{\Delta k} \tag{1-11}$$

this Hamiltonian is in the same form as the famous Dirac Hamiltonian $\mathrm{H} = \hbar c\vec{\sigma}\cdot\vec{k}$ in two dimensions, where σ is the Pauli matrices (Close to K', the Hamiltonian is $\hbar \mathrm{v}_F \vec{\sigma}^*\cdot\overrightarrow{\Delta k}$). In analogy with the real spin in Dirac equation, the two components of the wave function corresponding to the sublattice A and B is called pseudospin [1] and the Fermi velocity $\mathrm{v}_F = \frac{\sqrt{3}}{2}\frac{\gamma_0 \mathrm{a}_0}{\hbar} = 10^6 m/s$ which is 1/300 the speed of light. Within the Dirac cone, charge carriers in graphene behave like relativistic particles with an effective speed of light given by the Fermi velocity. This unusual

behavior in graphene brings the rich physics of quantum relativistic effects into the condensed matter field [4].

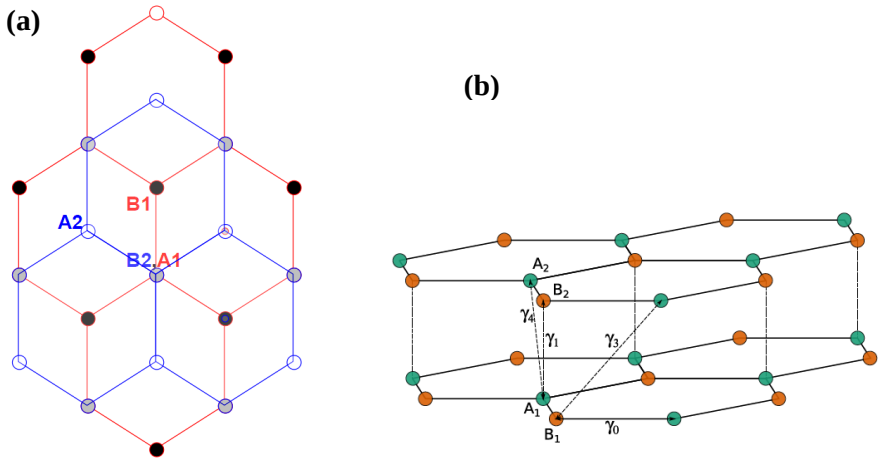

Fig 1-3 Lattice structure of bilayer graphene. (a) lattice structure in real space. (b) "hopping" parameters (adopted form [5]).

1.1.3 lattice and band structure of bilayer graphene

Bilayer graphene, as its name indicates, consists of two layers of graphene stacked together. Bernal (AB) stacking is the most common arrangement for bilayer graphene, the structure is shown in Fig 1-3a .The same tight-binding method can be used to solve the band structure of bilayer graphene, Fig 1-3b shows the possible hopping to nearest atoms in bilayer graphene and we have the Hamiltonian with the basis of components of wave function at sites A2, B2, A1, B1:

$$H = \begin{pmatrix} E_{\mathbf{k}} - E_0 & \gamma_0 f(\mathbf{k}) & \gamma_4 f(\mathbf{k}) & \gamma_3 f^*(\mathbf{k}) \\ \gamma_0 f^*(\mathbf{k}) & E_{\mathbf{k}} - E_0 & \gamma_1 & \gamma_4 f(\mathbf{k}) \\ \gamma_4 f^*(\mathbf{k}) & \gamma_1 & E_{\mathbf{k}} - E_0 & \gamma_0 f(\mathbf{k}) \\ \gamma_3 f(\mathbf{k}) & \gamma_4 f^*(\mathbf{k}) & \gamma_0 f^*(\mathbf{k}) & E_{\mathbf{k}} - E_0 \end{pmatrix} \tag{1-12}$$

Solving the eigenvalue equation will give us four bands. The typical value for hopping energy obtained from experiments are $\gamma_0 \approx 3\ eV$, $\gamma_1 \approx 0.1\,\gamma_0$, $\gamma_{3,4} \approx 0.03\,\gamma_0$ [5]. Here we consider only

the dominate terms with hopping energy γ_0 and γ_1 and look at the band structure near K. Then the two high-energy bands are given by [6],

$$E_2^{\pm} = \pm\frac{\gamma_1}{2}\left(\sqrt{1 + 4\hbar^2 v_F{}^2 k^2/\gamma_1} + 1\right) \tag{1-13}$$

and the two low-energy bands are given by,

$$E_1^{\pm} = \pm\frac{\gamma_1}{2}\left(\sqrt{1 + 4\hbar^2 v_F{}^2 k^2/\gamma_1} - 1\right) \tag{1-14}$$

the two low-energy bands sit in between the high-energy ones, and show a quadratic relation to k for low momenta and linear for high momenta (Fig 1-4)

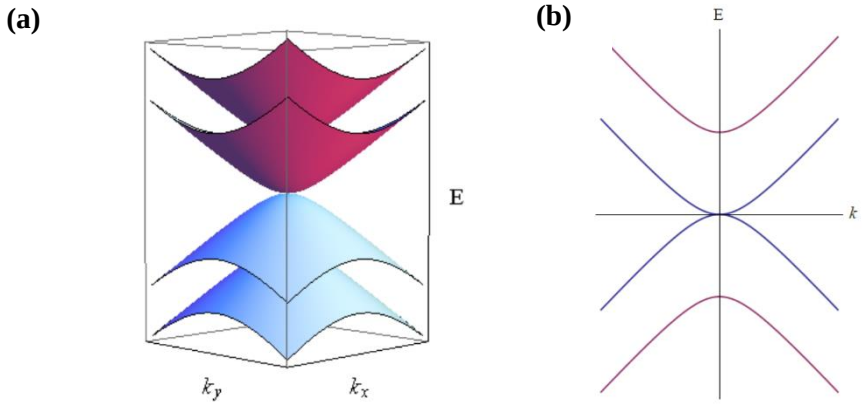

Fig 1-4 Band structure of bilayer graphene near K point.

1.1.4 moiré pattern in twisted bilayer graphene (tBLG)

Twisted bilayer graphene is attracting more and more attention since recent experimental work shows exciting results by controlling the twist angle to around 1.1°. In this section we will show the main feature of twisted bilayer graphene (tBLG) -- a flat band structure [7,8]

To describe the twist angle between two layers of graphene, the commensurate structure is often used in theoretical works and calculations [7~10]. We can rotate the second layer graphene with

respect to the first layer so that lattice vector $\mathbf{V} = m\,\vec{a} + n\vec{b}$ moves to $\mathbf{V}' = n\,\vec{a} + m\,\vec{b}$ to produce the Moiré patterns. Then **V** and **V'** will be the primitive lattice vectors of the moiré cell (Fig 1-5). and the rotation angle for such commensurate structure is given by

$$\mathrm{Cos}\theta = \frac{1}{2}\frac{m^2+n^2+4mn}{m^2+n^2+mn} \tag{1-15}$$

and we noticed that a small twisted angle is constructed for $m = n + 1$ with AA stacking locates at corners and AB stacking at 1/3 and 2/3 of the long diagonal [8].

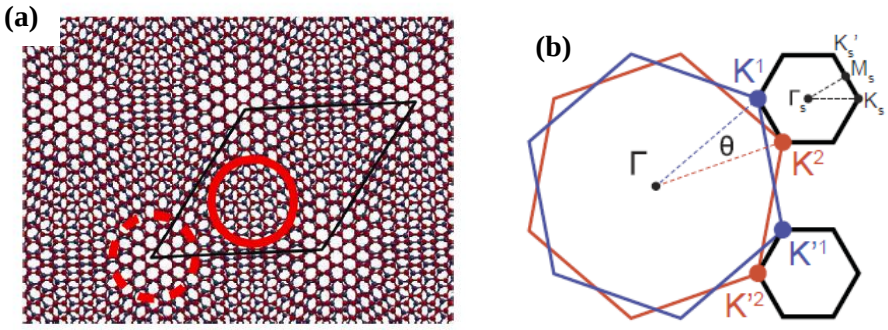

Fig 1-5 Moiré pattern of twisted bilayer graphene. (a) the primitive cell vectors of moiré lattice and illustration of AA and AB stack region (adopted from [8]). (b) k-space Brillouin zone of bilayer graphene and reduced Brillouin zone of tBLG.

1.1.5 band structure of tBLG

A simple picture for the band structure of tBLG is to understand it as folding the band of single layer graphene into the reduced Brillouin zone [9]. The low-energy band width is reduced to $4\pi\hbar v_F/3|V|$ and the Fermi velocity is reduced with the same scale. Such a picture works good for twist angles lager than 5°. However, at smaller twist angle, the band structure calculated from tight-binding method deviates from this picture [10]. The band width is significantly reduced and velocity tends to be zero near θ=1.08° [8].

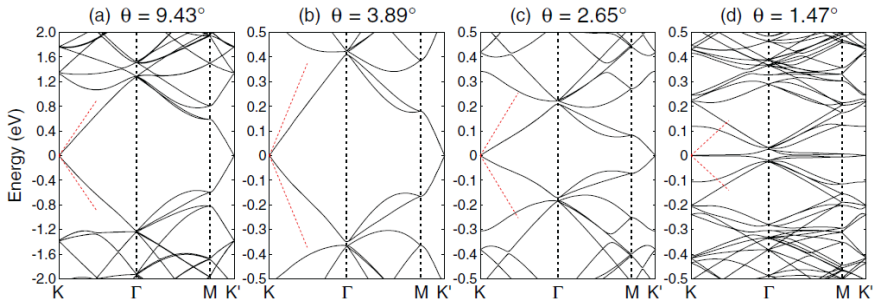

Fig 1-6 Band structure of tBLG [10].

The behavior at small twisted angle can be qualitatively explained as a competition between the kinetic energy and interlayer hybridization energy. The two Dirac cone K1 and K2 are from the K point of the first and second layer. At the position they overlap, a gap will form with energy 2*w*. As the twist angle θ decreases, K1 and K2 move closer and *w* will finally be comparable to the kinetic energy. As a result, the low-energy band will be flat, producing a Fermi velocity close to zero, leading to correlated insulating and superconducting states [11,12].

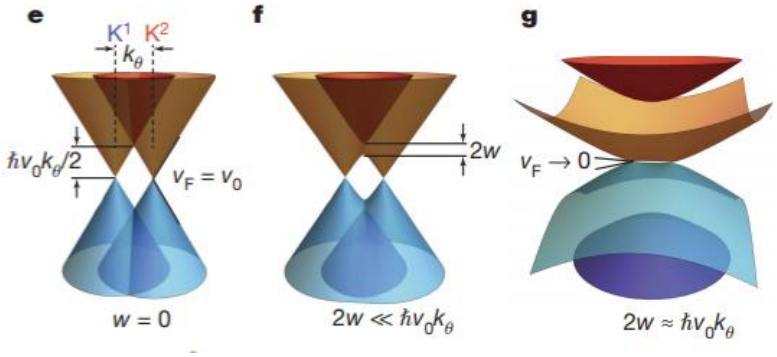

Fig 1-7 Illustration of competition between the kinetic energy and interlayer hybridization energy [11].

1.2 Integer Quantum Hall Effect

1.2.1 quantum Hall effect in two-dimension free electron gas

When uniform magnetic field is applied perpendicular to electrons in two dimensions, electrons will move in circular cyclotron orbits. By solving the Schrodinger equation for free electron in magnetic field, it is shown that the energy spectrum is quantized into discrete Landau levels (LL). As a result, properties such as conductivity, thermal conductivity, magnetic susceptibility etc. will show oscillatory behavior with magnetic field. In particular, the oscillation in conductivity, known as Shubnikov-de Haas oscillations (SdHOs) [13], can evolve into the Quantum Hall effect in appropriate samples under large magnetic field at sufficient low temperature. The quantum Hall effect was first observed by Klaus von Klitzing in 1980 [15], characterized as quantizing in units of $\frac{e^2}{h}$ of Hall conductivity together with vanishing of longitudinal conductivity. That is:

$$\sigma_{xy} = \nu \frac{e^2}{h},\ \sigma_{xx} = 0 \quad (\nu = 1,2,3,\dots) \tag{1-16}$$

To understand the behavior of 2D system under magnetic field, let's consider 2D electron gas. Without a magnetic field, the energy spectrum is given by

$$E(k) = \frac{\hbar^2 k^2}{2m} \tag{1-17}$$

And when a uniform magnetic field *B* perpendicular to the plane is applied, energy collapse into Landau levels given by

$$E_\nu = (\nu + \tfrac{1}{2})\hbar\,\omega_c \quad (\nu = 1,2,3,\dots) \tag{1-18}$$

$\omega_c = \frac{q\,B}{m}$ is the circular frequency of electron's orbit in semiclassical picture. In Fig 1-8, we see that the quasi-continuum energy spectrum quantized into highly degenerated Landau levels. For a sample with length of *L*, the degeneracy of each Landau level is

$$D = \frac{e\,L^2 B}{2\pi\hbar} \tag{1-19}$$

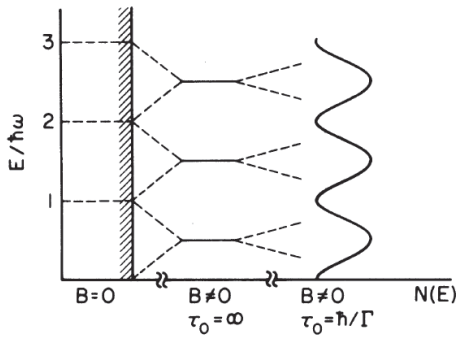

Fig 1-8 Landau levels in two-dimensional free electron gas [16].

Plateaus in σ_{xy} appears each time when a Landau level is fully filled. The number of electrons *N* in the sample is:

$$N = \nu D = \nu \frac{e\,L^2 B}{2\pi\hbar} \quad (\nu = 1,2,3,\dots) \tag{1-20}$$

and the Hall conductivity σ_{xy} is given by,

$$\sigma_{xy} = n\,e/\,B = \frac{N}{L^2} e/B = \nu \frac{e^{\,2}}{h} \quad (\nu = 1,2,3,\dots) \tag{1-21}$$

Lastly, it's instructive to rearrange Eq (1-19) in the following form:

$$B = \frac{h}{e}\frac{D}{L^2} = \Phi_0\, n/g \tag{1-22}$$

where $\Phi_0 = \frac{h}{e}$ is the magnetic flux quanta, n is the number of electrons in a unit area, and g is the degeneracy of the system. Eq (1-22) is a general condition for Landau levels in magnetic field and has a simple physical mean that the system will quantize into Landau levels that in each Landau level one flux quanta goes through one cyclotron orbit.

1.2.2 quantum Hall effect in graphene

As shown in previous section, the transport of graphene and bilayer graphene are governed by equations which differ from free electron gas. For monolayer graphene, Landau levels are given by solving Dirac's equation, and have the energy [1,16],

$$E_\nu = sgn(\nu)\sqrt{2\hbar v_F^2|\nu|eB} \quad (\nu = 0, \pm1, \pm2, \dots) \tag{1-23}$$

In experiment, the distinctions between graphene and normal 2D free electron system have been clearly observed. (1) The spin and valley degeneracy in graphene contributes a factor of g = 4 in Eq (1-22). (2) m_c, the effect cyclotron mass, was found to be proportional to $n^{1/2}$,where n is the carrier density [4]. Such a result proves that energy E is proportional to k. And even though graphene has a linear energy spectrum on k, which indicates zero rest mass, the cyclotron mass is given by the relativistic equation $E = m_c v_F^2$. (3) Furthermore, replacing the mass in $\omega_c = \frac{e\,B}{m}$ by $m_c = E/v_F^2$ and pluging into Eq (1-18), it is indicated that $E_\nu \propto \sqrt{\nu B}$, which agrees with Eq (1-23). (4) The plateau in σ_{xy} shifts by 1/2 compare to conventional quantum Hall effect and is given by

$$\sigma_{xy} = \pm(\nu + \tfrac{1}{2})\tfrac{4e^2}{h} \quad (\nu = 0,1,2,\dots) \tag{1-24}$$

the shift of 1/2 can be thought resulting from the Berry phase of π due to the precession of pseudospin as Dirac fermions undergo cyclotron motion [17,18]. Fig 1-9(c) is a schematic illustration of quantum Hall effect in monolayer graphene.

In bilayer graphene, energy of Landau levels is given by

$$E_\nu = sgn(\nu)\sqrt{|\nu|\,(|\nu|-1)}\,\hbar\,\omega_c \quad (\nu = 0, \pm1, \pm2, \ldots) \tag{1-25}$$

with $m_c \approx 0.03 m_e$, and m_e is the mass of electron. The quantum Hall effect in bilayer graphene is also unconventional and

$$\sigma_{xy} = \pm\nu\frac{4e^2}{h} \quad (\nu = 1,2,3,\ldots) \tag{1-26}$$

the plateau for ν = 0 is "missing" because of the Berry phase of 2π. The system degeneracy of bilayer graphene is g = 4, but a perpendicular electric field can break the degeneracy and cause the splitting of Landau levels in low magnetic field. Fig 1-9(b) shows the quantum Hall effect in bilayer graphene.

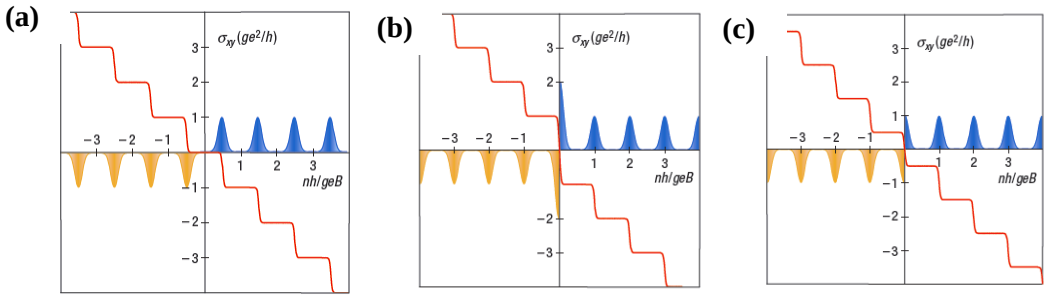

Fig 1-9 Schematic illustration of quantum Hall effect for (a) 2D free electron gas. (b) monolayer graphene. (c) bilayer graphene (adopted from [17]).

Chapter 2 Device Fabrication

2.1 Mechanical Exfoliation of Layered Materials

For materials like graphite and hexagonal boron nitride (hBN), layers are bonded by the van der Waals force. It is easy to cleave them by an external force. There are early works that use atomic force microscope (AFM) or scanning tunneling microscope (STM) tip to get every thin graphite flakes [19,20]. Furthermore, these layered materials can be cleaved and isolated down to a thickness of a few atoms, even only one atomic layer in thick, by the "mechanical exfoliation" method [21]. Two-dimensional (2D) materials obtained by the mechanical exfoliation method have rather high quality, and defect in the material can be controlled to its minimum. For this reason, it is very suitable for studying the intrinsic properties of these material and exploring some fundamental effects in physics.

2.1.1 procedure of exfoliation with scotch tape

To get graphene and few layer hBN flakes used for fabricating high-quality devices, we start with the bulk materials. Examples of these layered bulk materials are Kish graphite, Highly Ordered Pyrolytic Graphite (HOPG), synthesis hBN and BN powder. For simplicity, I'll use Kish graphite as an example, and the procedure for exfoliation of other materials are similar. First, several Kish graphite flakes was attached on the scotch tape. Then we fold the tape in different directions so that

graphite flakes were “copied” by two in each folding until they cover almost the whole area that we want to place Si/SiO_2 wafer on later. By firstly spreading graphite on a single tape , we can reduce the chance that tape residue is transferred onto the 2-D material. And after this “mother” tape is made, we repeat the procedure of attaching and releasing the prepared tape with a new one until the “density” of the flake on the tape is proper for the next transfer. A proper “density” of the flake differs for different materials, and it’s hard to characterize in quantitatively. But with enough practicing, it’s relatively easy to get an idea about it.

In the next step, the tape is placed on the clean Si/SiO_2 chips. Si chips with a 290nm oxidized SiO_2 layer is used to give good contrast in identifying graphene under optical microscope. We gently press the tape to squeeze out air bubbles, and then hold the chip and slowly peel the tape from one side. With a proper “density” of flakes on tape, some mono- and few-layer graphene will be transferred onto the chip.

Next, we use optical microscope to determine the number of layers of graphene flakes and figure out those with proper size and thickness we need. Monolayer, bilayer and tri-layer graphene show different colors under an optical microscope Fig 2-1, which can be seen by naked eye. However, the difference in color is smaller as the number of layer increases. Telling the exact number of layers for thicker graphene flakes with an optical microscope is hard. In this case, one may use AFM or Raman spectroscopy [21, 22] if needed (and obviously, the AFM and Raman spectroscopy is also valid in identifying mono-layer bi-layer and tri-layer graphene).

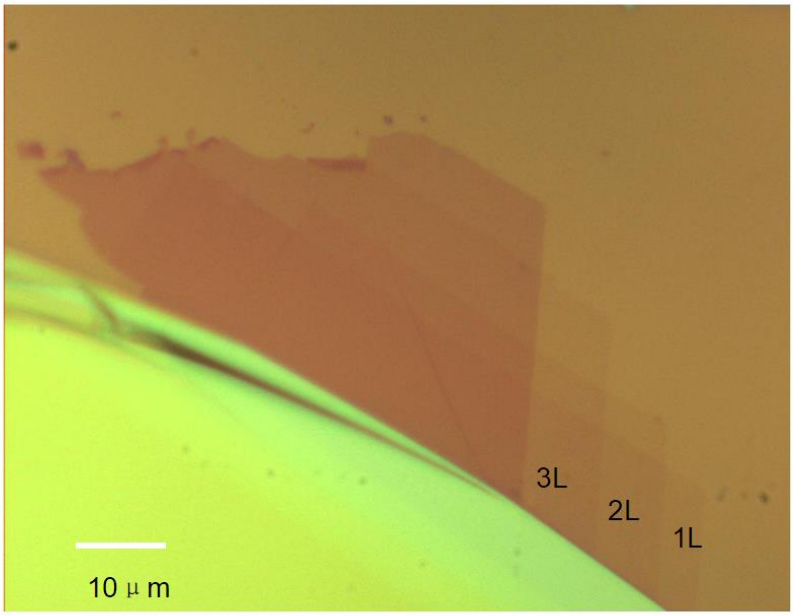

Fig 2-1 Optical image of graphene with thickness of 1~3 layers.

For hBN, if the exact thickness is not crucial, as is the case for most devices in this dissertation, the color of the flake can give a satisfactory estimation on the thickness. For our devices, we use hBN that shows a bluish to green color, and the thickness at such color range is 20~50 nm based on AFM measurements.

Finally, furnace annealing is done to remove any tape residue on the chip. Although this step is sometimes optional, and even inapplicable for air sensitive materials, we found by performing this furnace annealing step, the defects in devices can be reduced, thus improving the quality of device. A discussion about this is given in Chapter 3. The recipe for furnace annealing is shown is Table 2-1.

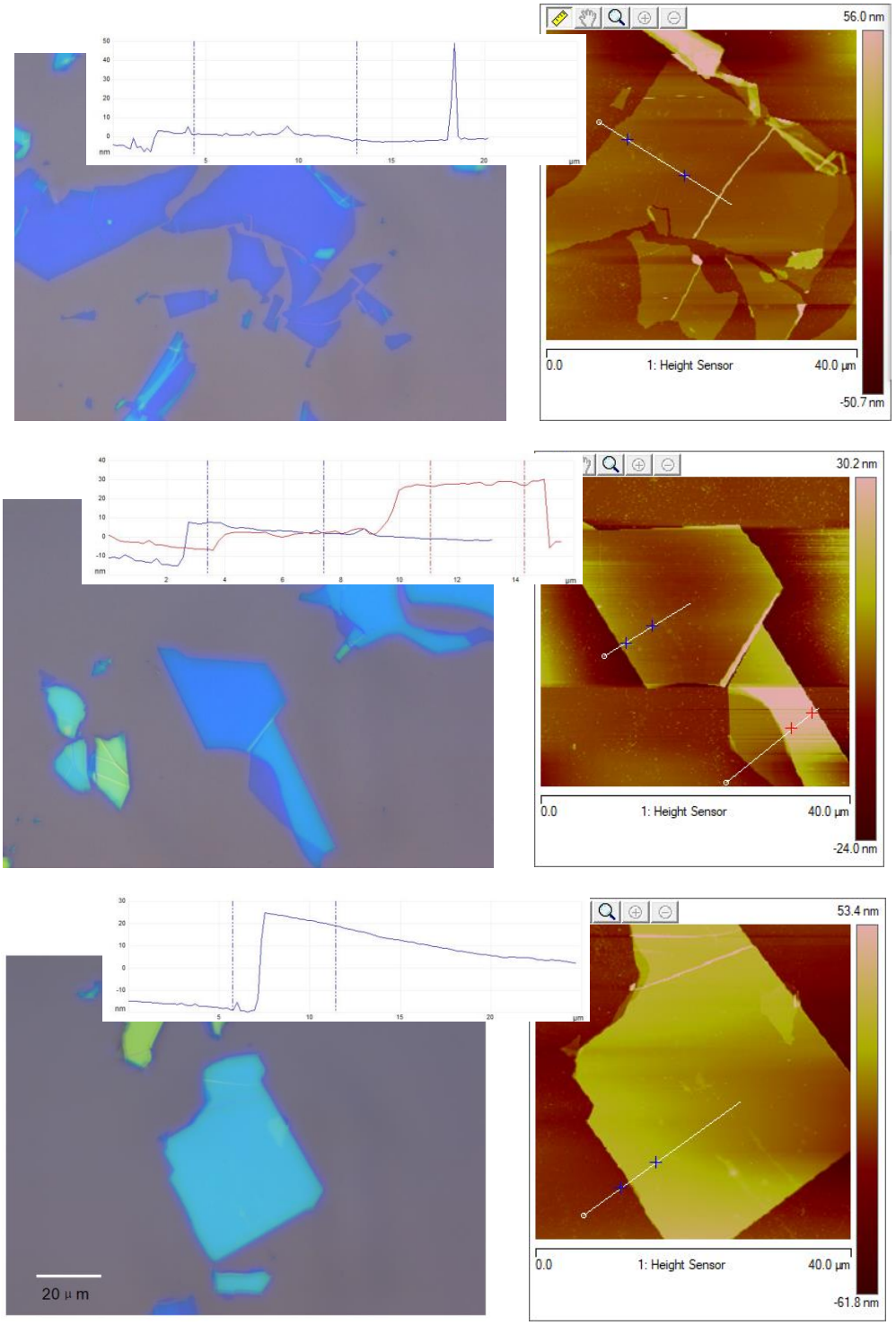

Fig 2-2 Optical and AFM image of hBN.

Table 2-1

Furnace annealing for graphene (hBN) fakes: O_2 at flow rate of 0.5~1 standard cubic centimeter per minute (sccm), at temperature 300℃ (500℃).
Set point for graphene (hBN) is 300 ℃ (500℃) t0~t1: 15min (20min) t1~t2: >3hr furnace is power off after t2   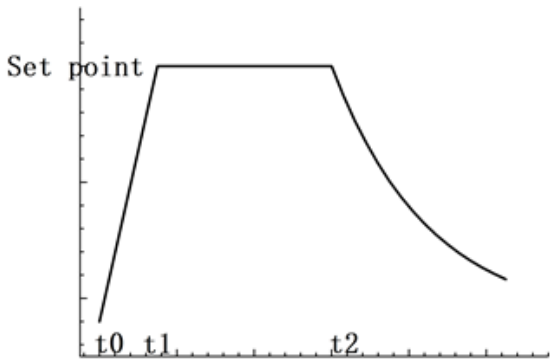

2.1.2 graphene prepared by razor blade scratching

Besides the regular exfoliation procedure with scotch tape, we also use graphene flakes obtained by the "razor blade" method to fabricate devices: first, thick graphite flakes are deposited on pre-cleaned Si/SiO_2 chips. Then, instead of repeating exfoliating the fake with scotch tape, we use the tip of razor blade to gently scratch on the flake. As part of the flake is scratched off from the chip, the rest of the flake is "exfoliated" at the edge by the razor blade and chances are that a large graphene piece is left at the boundary. Fig 2-3 shows large monolayer and bilayer graphene obtained by this method. The advantage of using a razor blade to perform the mechanical exfoliation is that the graphene can be kept free from any tape residue. Both AFM and transport measurements show that the stack made with "razor blade" graphene is cleaner compared to the regular "scotch tape" graphene. Detailed results are discussed in section 3.2.3 and 3.3.

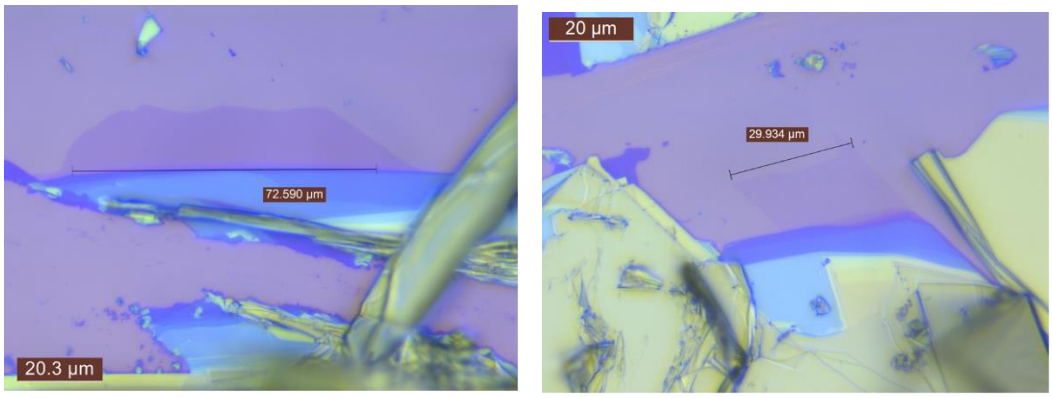

Fig 2-3 “Razor blade” graphene, left: bilayer, right: monolayer.

2.2 Dry Transfer Method for Making van der Waals Heterostructure

After having graphene and hBN flakes on the chip, the next step is to assemble them into a stack. The method we use here is called the “pick-up” method, and is first proposed by L. Wang [23]. The pick-up method provides a huge flexibility in making devices with 2D materials. In principle, we can stack different 2D materials on top of each other in any order and as many times as we want, which is just like assembling Lego in atomic scale [24]. What’s more, using the “tear-and-stack” strategy based on the “pick-up” [25, 26], Cao and Kim’s work opens the possibility of controlling the twist angle -- relative crystal orientation between different layers of the stack. The precise control of twist angle provides a new way to modify the properties of materials and in twisted bilayer graphene, it has led to some surprising new findings originated from the “magic angle” [8,11,12]. A detailed procedure of making twisted bilayer graphene stack is illustrated below as an example of the pick-up method:

1.Prepare the transfer glass slide

Starting with a glass slide, we first apply a layer of transparent tape on it. This layer of tape was then cut into small squares of ~2 mm × 2mm. Multiple squares can be made on one glass slide and these squares serve as a stamp for transfer (Fig 2-4). Then, a second layer of transparent tape is attached on the glass slide to cover the stamps. Next, we spin coat polypropylene carbonate (PPC) onto the glass slide to finish the transfer glass slide (The recipe for dissolving and spin coating PPC is shown in Table 2-2.

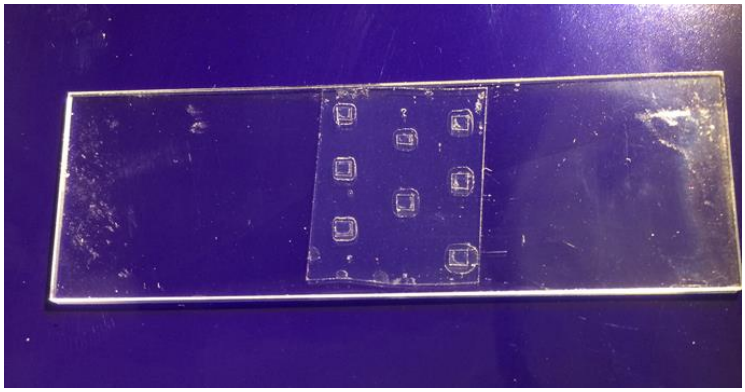

Fig 2-4 Picture of a glass slide with transfer stamps.

2. Pick up top hBN from chip

We place the glass slide on the X-Y stage of the microscope and a chip with the hBN we want to pick up is mounted on a micromanipulation stage which can move on all three translation dimensions and pitch and yaw angles. The PPC and the flake are placed face to face. More details of the transfer stage setup are given in next section. To pick up the top hBN, we align it with a stamp on the glass slide and heat up PPC to 40℃, which gives the best adherence to flakes. When

lowering the transfer stage, a stamp will touch the flake on the chip first and provide a good contact between PPC and the flake. After the whole flake is in touch with PPC, we quickly retract the micromanipulator, and hBN flake will be picked up.

Table 2-2

PPC solution: poly-propylene carbonate (Sigma-Aldrich, CAS 25511-85-7) is dissolved in anisole at a ratio in weight of 1.5 : 8.5 (15% in weight). The beaker is placed on hot plate at 60℃ and stirred overnight to fully dissolve PPC.
Spin coat: PPC is spin coated on tape at 6500 Revolutions per minute(rpm) for 45 seconds. Then the glass slide is place on hot plate at 100℃ and baked for 10 min.

3. Tear and stack graphene, pick up bottom hBN

The next step is to use the top hBN to pick up the following layers of the stack. Due to the fact that the van der Waals force between 2D flakes is much stronger than the force between a flake and the Si/SiO2 chip, we can bring the top hBN close to a graphene flake on the chip and use the van der Waals force to pick it up. Here, the tear-and-stack strategy is also needed to make the twisted bilayer graphene. To do this, we first partially align the top hBN with graphene, which means we only bring half of the graphene in contact with hBN when lowering the stage. In contrast with the previous step, for the following pick-up we always first bring PPC and the chip in contact and then heat PPC. The PPC is heated to 60~90℃, and at this temperature range, PPC is softened and tend to press on the chip due to thermal expansion. As a result, hBN and graphene under it will attract and form a stack. To avoid PPC from sticking on the chip, we wait for PPC to cool down to room temperature and then retract the stage. The van der Waals for is so strong that the graphene will be torn along the edge of the stack, leaving the other half of graphene flake on the chip. Since this flake has same crystal orientation as one on our stack, we can change the relative crystal orientation

between the two layers simply by rotating the micromanipulation stage and repeat the pick-up procedure. Finally, the bottom hBN is pick-up by repeat the procedure again.

4. Drop the stack onto chip

The glass slide with the stack and a chip with pre-patterned alignment marks are placed in the same way as previous steps. We bring the stack to the chip and heat PPC to ~120℃. This temperature will melt PPC and we retract the micromanipulation stage and leave the stack and PPC on the chip. Then the chip is dipped in chloroform for 1 min to dissolve PPC. And the stack is successfully placed on the chip with alignment marks and ready for the standard e-beam lithography procedure. Fig 2-5 shows a schematic diagram of the pick-up method.

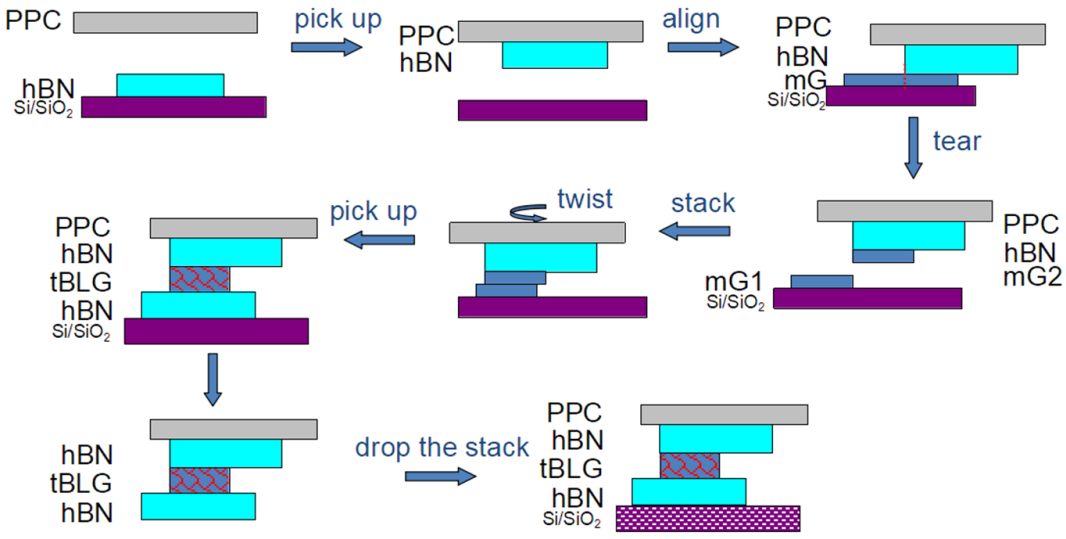

Fig 2-5 Schematic diagram of the pick-up method.

2.3 Apparatus for Transfer

Fig 2-6 and Fig 2-7 shows the microscope and micromanipulator we use for transfer procedure. The x-y stage on microscope is used to coarsely align flake with the stamp and then keep fixed during transfer procedure. The micromanipulator we use provide a precise control of three translation direction and two direction of rotation Fig 2-7. We can't change the third direction of rotation continuously, but in practice, it can be manually adjusted to meet the requirement for our experiment.

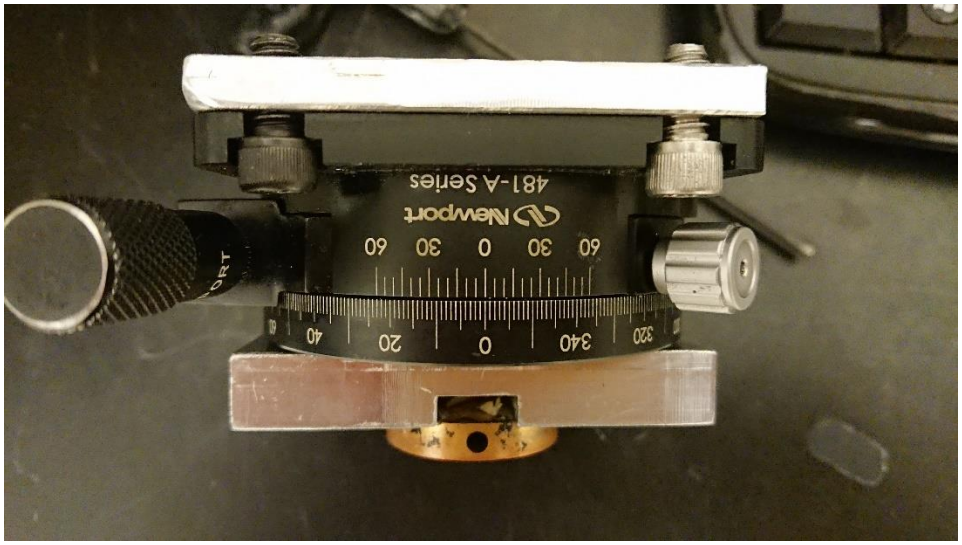

Fig 2-6 micromanipulator 1.

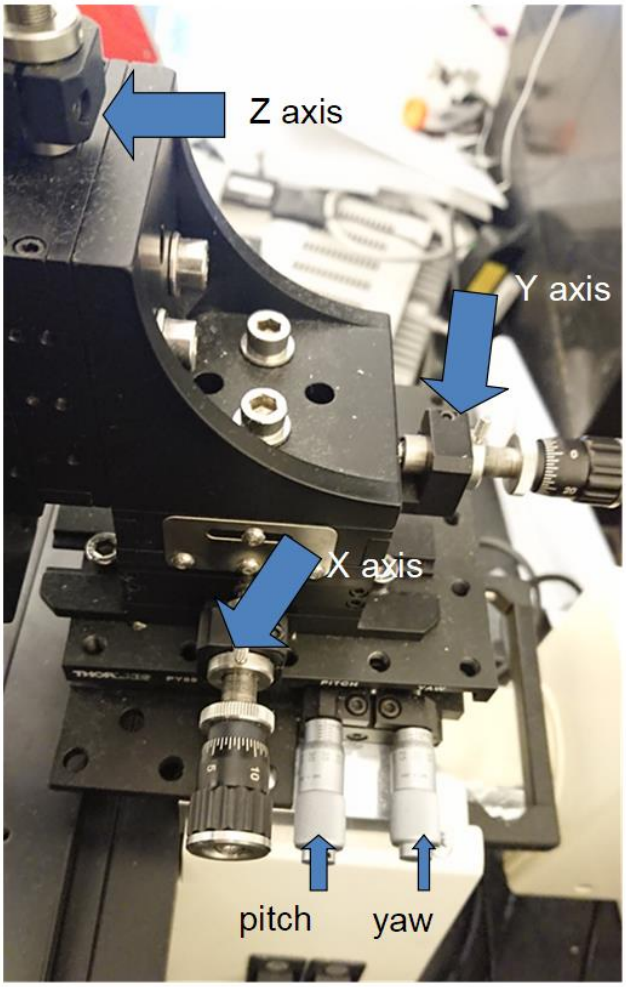

Fig 2-7 micromanipulator 2.

We also have a script to assist us in the transfer procedure. The script provides the function of detecting the edge of a saved image and overlapping it with the live image from microscope. The saved edge contour can be moved and rotated to help us align flakes during transfer. The use of the script is illustrated in Fig 2-8.

(a)

(b)

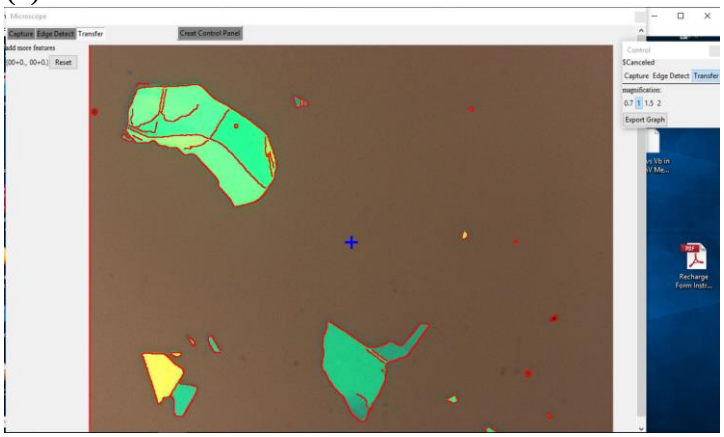

(c)

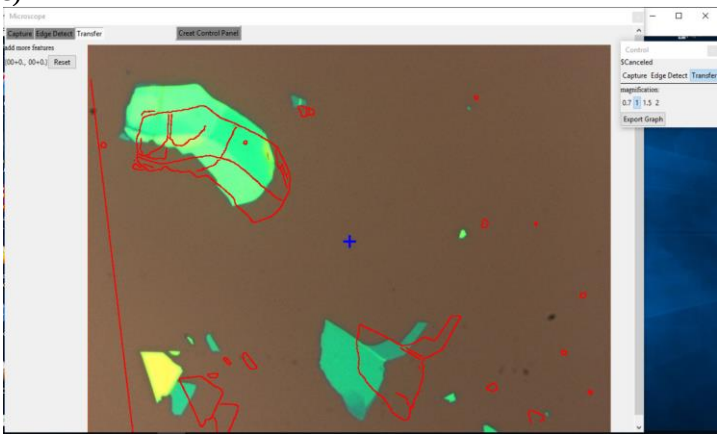

Fig 2-8 Screen shot of the script used for (a) detecting edge. (b) overlapping to microscope image. (c) adjusting edge contour position.

2.4 E-beam Lithography and RIE

we use standard e-beam lithography (EBL) procedure and reactive ion etching (RIE) to define the geometry of the device and make quasi one-dimensional contacts to the edge of graphene. In this procedure, at least two rounds of lithography are needed. In the first lithography round, we define the device into a hall bar geometry and use RIE to etch the pattern. In designing the hall bar pattern, we intentionally make the leads a bit longer than we actually needed to protect the contact edge from polymer residue. In the second round of lithography, we define the electrodes and bounding pads. This time our pattern for electrodes expose the extra lead on the hall bar. And again we use RIE to etch away the extra leads. By doing this, we can make a clean quasi one-dimensional edge for metal contact. In the work of L. Wang [23], where the one-dimensional contact is first proposed, they directly etch a hall bar pattern, and before making metal contact, perform an O2 plasma cleaning to "flush" the edge. Here, we modified it into this sacrifice leads method. We find this can provide a more reliable contact on graphene because no polymer is possible to deposit on the contact edge. Finally, we use e-beam evaporator to evaporate Cr/Au contact on the device. The recipes for e-beam lithography, RIE, and e-beam evaporation is shown in table 2-3. And dose test for e-beam lithography and related metalization of the pattern is shown in Fig 2-9. And a summary of the completed procedure is listed in Table 2-4.

Table 2-4

Resist polymer for EBL: two layers of PMMA 950A. are spin coated on chip at 4000 rpm for 45s. Chip is baked on hot plate at 180℃ for 10 min after each layer is spin coated.
RIE: a mixture gas of CHF_3 and O_2 is used for etching. The flow rate is 45 sccm and 5 sccm respectively. Under the pressure of 20mT, RIE power of 50W, the etch rate for hBN is ~50nm/min while the rate for graphene is much lower (~2nm/min).
E-beam evaporation: electrodes of Cr/Au are made as the edge contact to device. The evaporation is done at the pressure less than 5×10^{-7} tor. The thickness of Cr/Au is 5/80 nm. For Cr, the rate of evaporation is ~1 Å/sec and for Au, ~2.0 Å/sec

Table 2-5

Summary of EBL and e-beam evaporation procedure
Alignment marks are made by EBL on clean chips. Cr/Au of 5/50 nm in thick is evaporated using e-beam evaporation. Chips are furnace annealed at 300℃ in O_2 for 3 hr to remove polymer residue before stack is transferred on.
Stack is made using pick-up method and transferred on the chip with pre-patterned alignment marks.
EBL is done to define the stack into specific pattern (for example, the Hall bar shape). RIE is used to etch the pattern. Then chip is soaked in acetone for >3 hrs to remove polymer residue.
EBL is done to define electrodes and bounding pads. RIE is used to expose the edge for contact. And Cr/Au of 5/80nm is made by e-beam evaporation.
Chip is soaked in acetone for >12 hrs to lift off extra Cr/Au. Usually, a longer time for soaking is helpful for lifting off the film. And small pieces of Cr/Au that is not lifted off may be removed by a careful sonication of 1~3 sec.
An optional top gate can be made by EBL followed by e-beam evaporation of Al_2O_3/Cr/Au of 200/5/80 nm. A thick layer of Al_2O_3 is required here to fully cover the height of the device and electrodes to avoid shorting to electrodes. And a similar lift-off procedure is done afterwards.

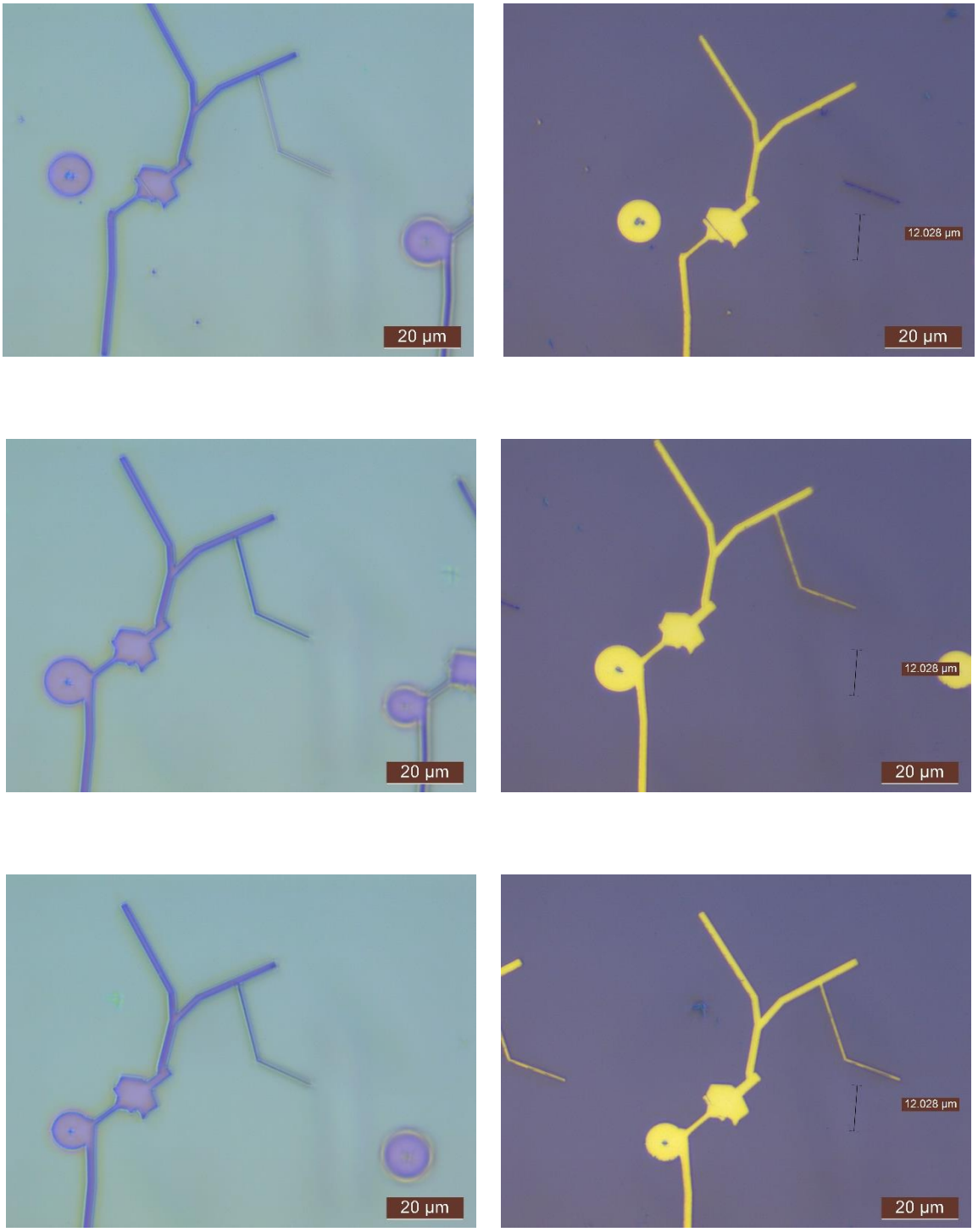

Fig 2-9 Dose test and metallization.

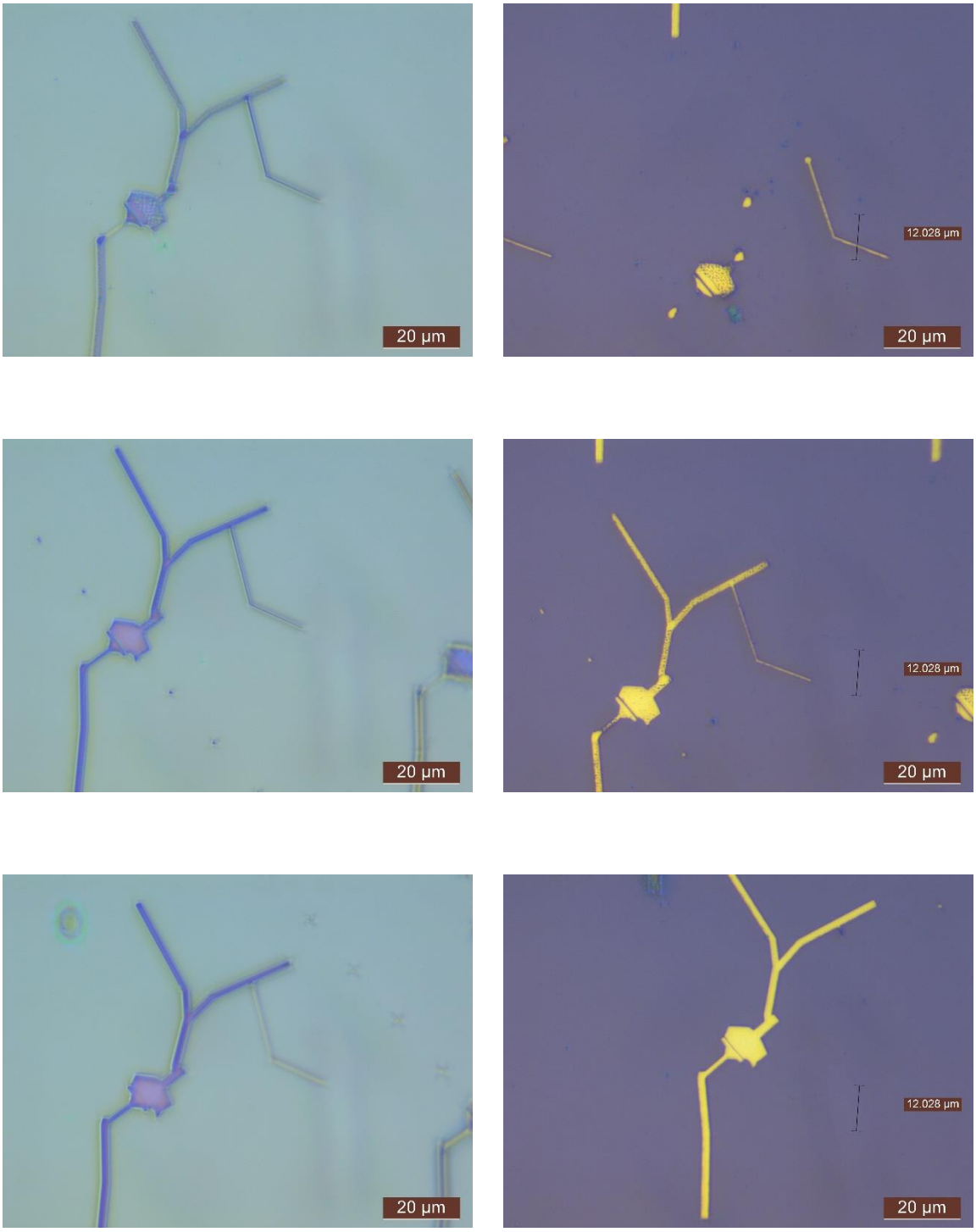

Fig 2-9(continued) Dose test and metallization.

Chapter 3 Characterization of van der Waals Heterostructures

3.1 Raman spectroscopy

Raman spectroscopy is a useful tool to characterize properties of two-dimensional materials. In early research of graphene, it is used to give an unambiguous identification of graphene layers [27]. Now Raman spectroscopy has become a more versatile tool in identifying disorder and defect, orientation of crystal, edge type, alignment of layers of heterostructure and measuring doping, strain, oxidation and so on [28-33]. Raman spectroscopy measurement is nondestructive, so it can be integrated with multiple research fields. In our work, Raman spectroscopy measurement is performed between steps of device fabrication to check the properties of the heterostructure.

Raman spectroscopy measures the shift in energy of laser photons that results from laser light interacting with phonons or other excitations in the system. Fig 3-1 shows the typical Raman features in graphene. The most prominent features in the Raman spectra of graphene are called the

G band, which appears at ~1582 cm^{-1}, and the G' band, which appears at ~2700 cm^{-1}. There is also the disorder induced the D band at ~1350cm^{-1} and D' band at ~1620cm^{-1} in the spectrum. The D and D' band can be observed in a disordered graphene sample or from the spectrum taken at the edge of a graphene sample. The G' band is also called 2D band in some text because its shift in wavenumber is about twice of the D band. However, the scattering process in G' band does not involve in any defects. Both the D and G' bands originate from the second-order process and exhibit a dispersive behavior as a function of the energy of the incident laser. More details about the phonon modes and Raman processes are not discussed here and can be found in [34].

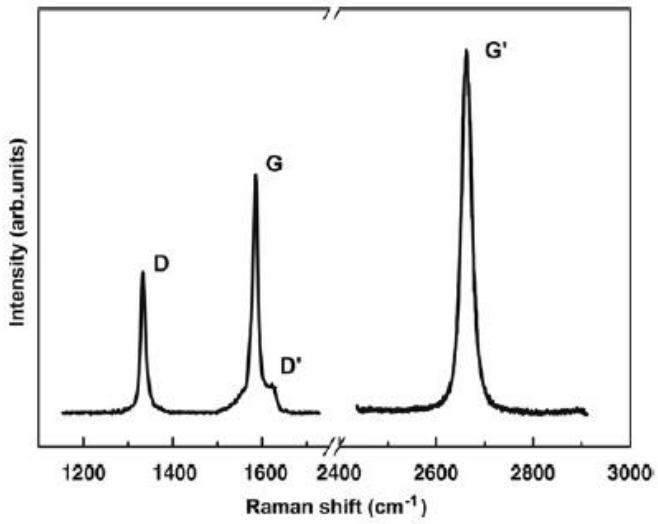

Fig 3-1 Raman features of graphene.

The relative intensity and the shape of the G' peak is often used in identifying the number of layers in graphene. The intensity of G peak increases linearly with the number of layers for few-layer graphene (layer number < 10 [35]). The shape of G' peak is closely related to the band structure of graphene, which varies with the number of layers. For monolayer graphene, the G'

peak exhibits a single Lorentzian feature, while for bilayer, the spectra can be fitted with four Lorentzians that related to the splitting of valence and conduction bands in bilayer graphene [5]. Similarly, tri-layer graphene can be fitted with six Lorentzians (Fig 3-2(b)).

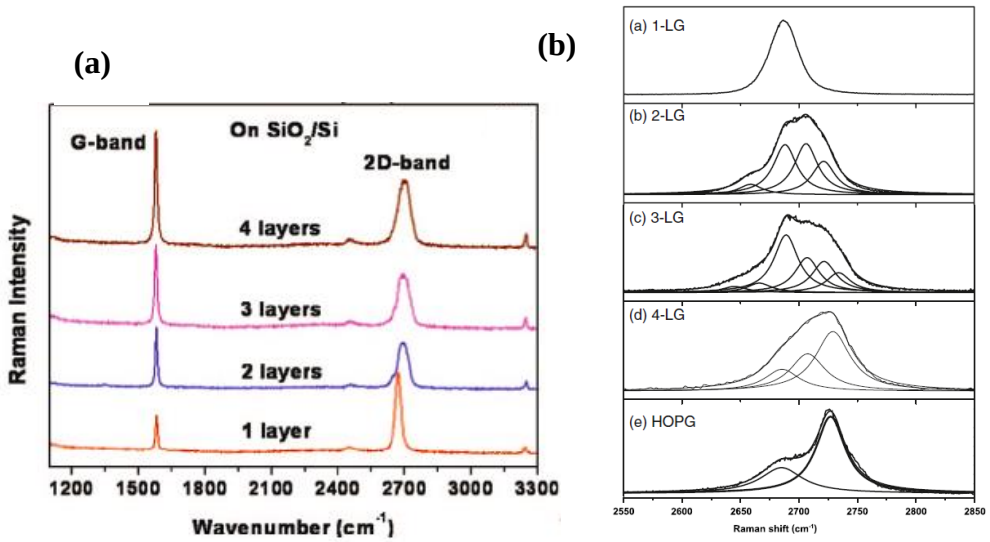

Fig 3-2 Layer dependence of Raman spectra in graphene (adopted from [36, 34]).

In our work, we use Raman spectroscopy to identify mono-layer and bilayer graphene. A sample of Raman spectra is shown in Fig 3-3(a). The laser with wavelength of 532nm used for measurement. And the laser power used is less than 1mW to avoid damage on the sample. Our measurement result agrees with the reported data [27]. The G peak is found at ~1580 cm^{-1} and G' is at ~2665 cm^{-1} for mono-layer graphene. It can be clearly seen that both the ratio between G and G' peak and the shape of G' peak give good evidence in telling the number of layers of graphene. There are few defects in exfoliated graphene, so the D and D' peak is in absence in most of the measurement. And it's worth mentioning that for tri-layer and thicker graphene, the shape of G'

peak is more complicated in that the peak varies not only with the number of layer but also the stacking order (ABA or ABC). Details of Raman spectroscopy of tri-layer and thicker graphene are not discussed here. Research on few-layer graphene with different stacking order can be found in [37,38]

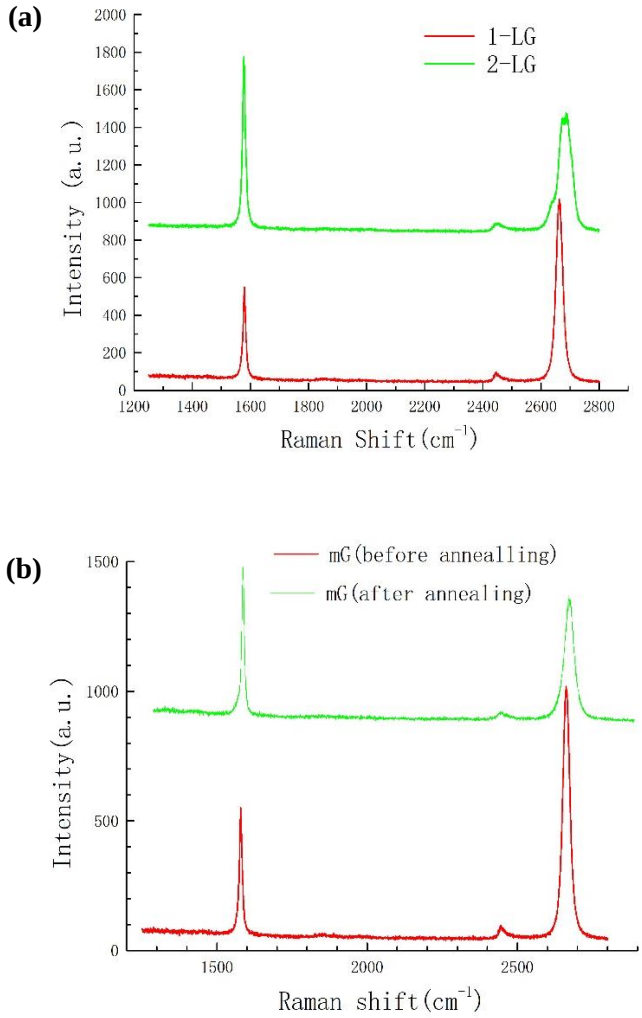

Fig 3-3 Raman spectroscopy of monolayer and bilayer graphene.

We also checked the Raman spectra of graphene sample before and after annealing (See sec. 2.1.1 for detail of furnace annealing procedures). The result is plotted in Fig 3-3(b). The ratio between

G and G' peak changes after annealing. We attribute this to the change of strength that graphene attaches to SiO_2 surface. It is shown that the intensity of G peak is related to the interference effects between graphene and the underlying substrate [35]. In addition, the strain in graphene also influences the position and intensity of G and G' peak [39]. Furnace annealing can remove hydrocarbons and tape residue attached on surface of graphene and release possible strain between graphene and SiO_2. These effects can all be sources that possibly affect the Raman spectra. But a quantitative understanding requires a more careful investigation and is beyond the topic of this dissertation.

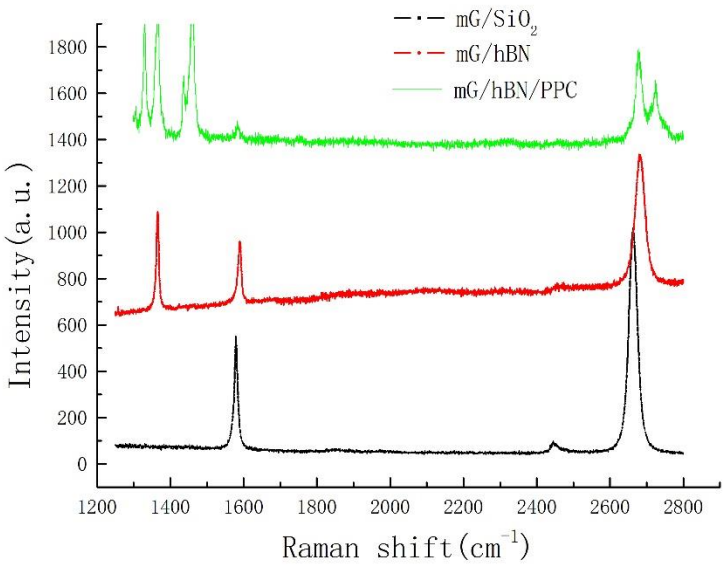

Fig 3-4 Raman spectroscopy of graphene on hBN.

In Fig 3-4, we investigate the Raman spectroscopy of graphene on hBN. The measurement is performed for stacks on PPC stamp during pick-up procedure and for stacks on Si/SiO_2 chip that flipped from the polymer stamp (see next section for steps to flip a stack). The Raman spectra

includes features from hBN and PPC, but the G and G' can still be easily identified. And the shift of ~20 cm^{-1} in G' peak is observed as the effect of hBN substrate.

Raman spectroscopy measurements can also be applied to twisted bilayer graphene samples. The Raman spectra of tBLG has been reported in samples that is folded [40, 41] or intentionally twisted by transferring two monolayer graphene together [42-44]. Theoretical calculation results can also be found [40, 45]. The Raman spectra of tBLG retains some features of monolayer graphene, but the G' peak shows a shift to larger wave number. At small twisted angles, the full width at half maximum (FWHM) of G' peak is slightly smaller than that of monolayer graphene. While for larger twisted angle, the Raman tends to recover to the case of two separated monolayers due two the weaker coupling between the two layers. The G peak shows a similar behavior, however, at certain twisted angle an enhancement of the G peak of more than 30-fold increasement can be observed. Additional peaks, R and R', are also reported in Raman spectra of tBLG at ~1375 cm^{-1} and ~1620 cm^{-1} respectively. Fig 3-5 is a brief summary of the reported Raman spectra of tBLG.

A better understanding of the angle dependence of Raman features in tBLG requires an investigation from theoretical aspect. Some reported results are shown in Fig 3-6. Experiment and the calculation results agree well, indicating that we have good explanations for Raman spectra of tBLG. On the other hand, unlike the case of monolayer and bilayer graphene, extraction of the twist angle from the Raman spectra remains to be a very hard task. The accuracy is limited by the relatively weak signal of the Raman features and the fact that angle dependence of the Raman spectra has no significant change with twisted angle in most cases.

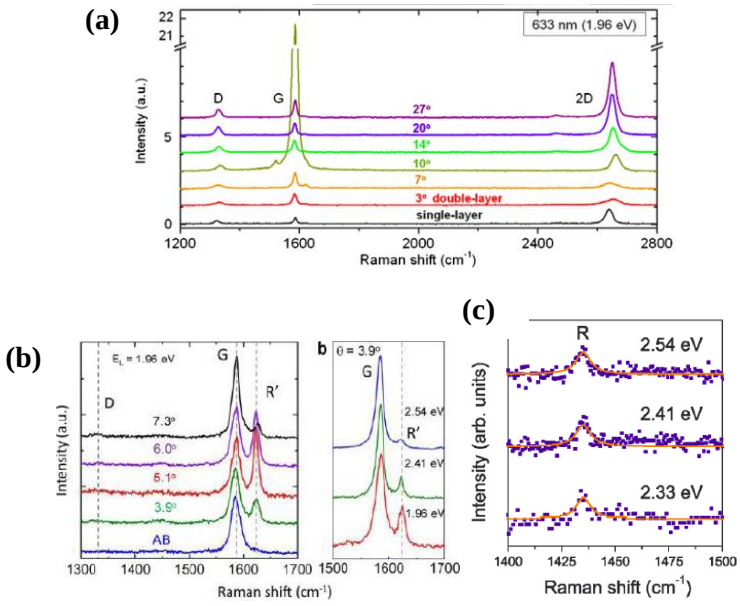

Fig 3-5 Overview of experimental data of Raman spectra of tBLG (a) angle dependence of Raman shift in the range of 1200 to 2800 cm^{-1} [42]. (b) R' peak for different angle and laser energy [43]. (c) the R peak in tBLG for twisted angle of $(15\pm2)^\circ$ [40].

In our experiment, we measured the Raman spectra of tBLG sample with the twisted angle of ~12°. At such a twisted angle, the energy difference between conduction and valence van Hove singularities reaches the energy of laser light for measurement. The energy difference (Fig 3-7) is given by,

$$\Delta E = \hbar v_F \, \Delta k \approx \hbar v_F \, \frac{4\pi}{3\,a}\theta \tag{3-1}$$

the enhancement happens when ΔE equals the photon energy of the laser used in measurement. In our experiment, we use 532nm laser, which has the laser energy of 2.34 eV. To match it with the energy difference mentioned above, $\Delta E = 2.34$ eV gives the twist angle of 11.9°.

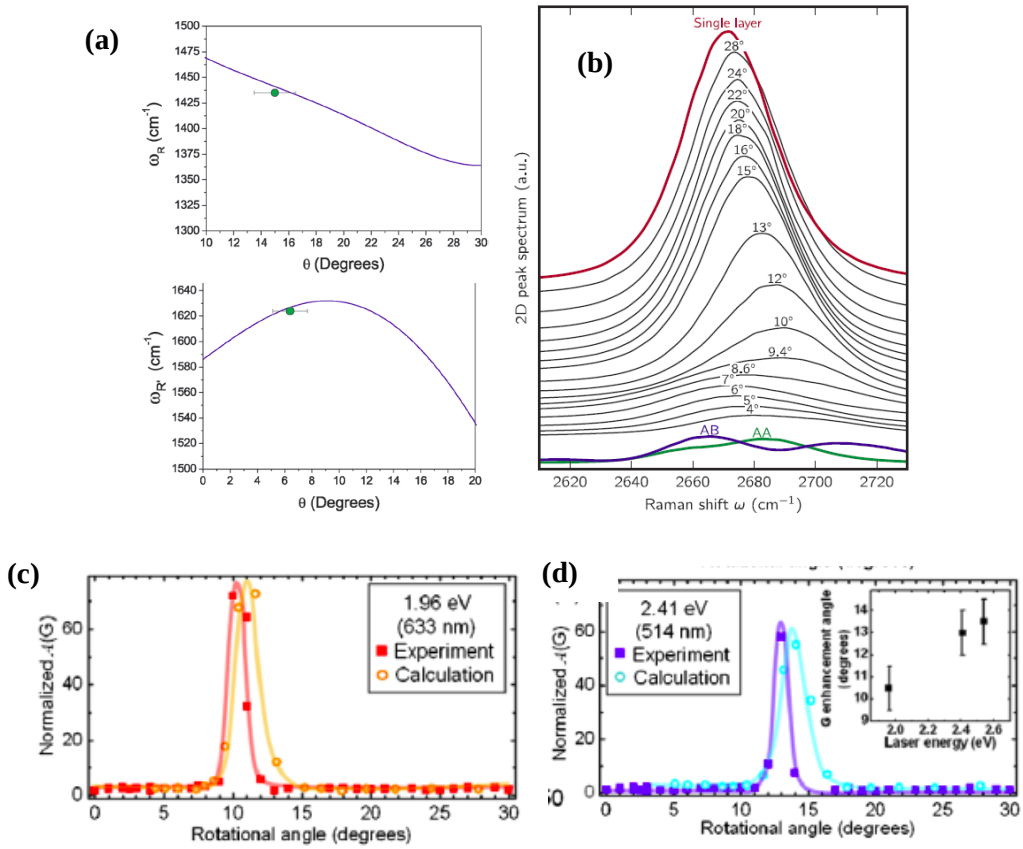

Fig 3-6 Overview of calculation and fitting of Raman spectra (a) the position of R and R' peak. (b) the angle dependence of 2D(G') peak. (c) and (d) fitting of intensity vs twisted angle for G peak with different laser energy. ((a) is adopted from [40], (b) from [45], (c) and (d) from [42]).

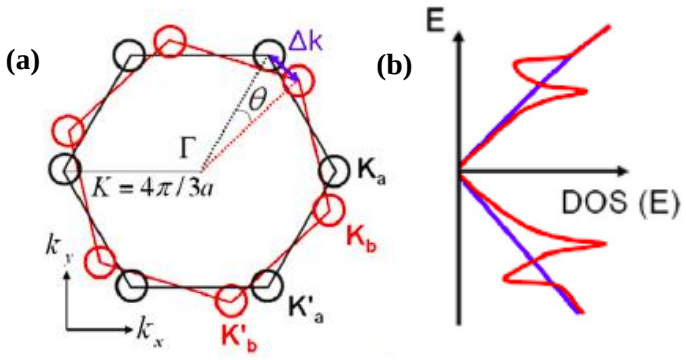

Fig 3-7 (a) Brillouin zone (BZ) of tBLG. (b) illustration of van Hove singularities in the sketch of density of states (DOS) for tBLG (adopted from [42]).

We checked samples of tBLG/hBN stack on PPC stamp and flipped tBLG/hBN stack. The measurement result in shown in Fig 3-8.

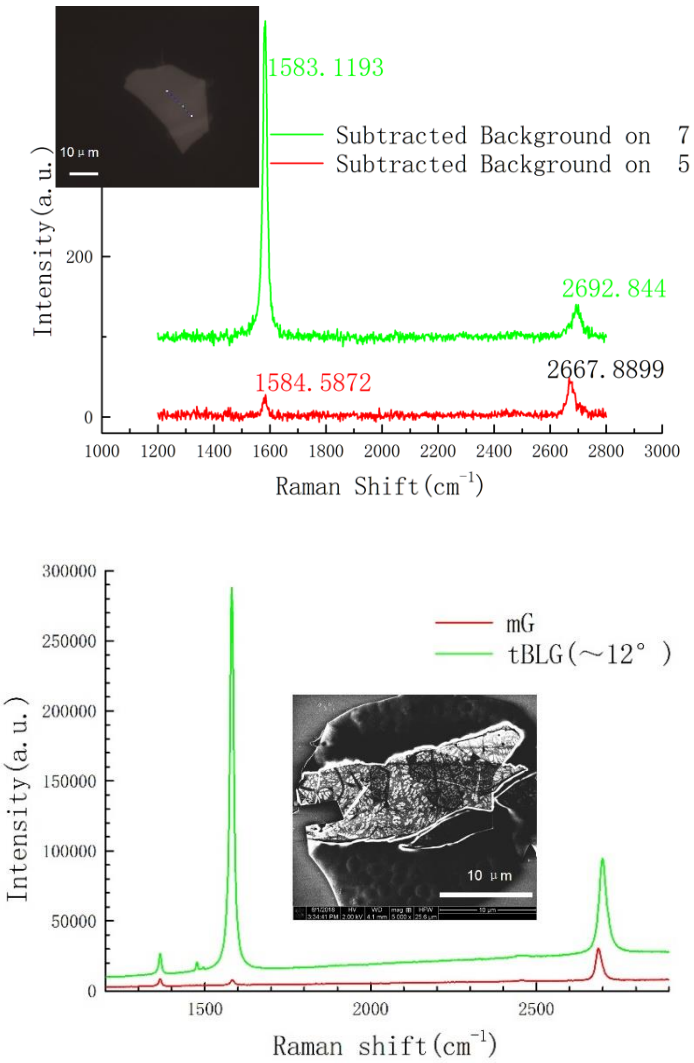

Fig 3-8 Raman spectra of tBLG with twist angle of ~12°. (a)tBLG/hBN stack on PPC stamp. Inset is the optical image of the sample. (b) tBLG/hBN stack on Si/SiO_2 chip. Inset is the SEM image of the sample.

For a sample on PPC stamp, we perform Raman spectroscopy measurement along a line on the sample (see inset of Fig 3-8 (a)) and identify the spots related to monolayer graphene and tBLG. The Raman features of PPC and hBN are removed by subtracting the measured spectra from the Raman spectra at the spot of hBN that is not covered by graphene on the same sample. And as expected, the enhancement of the G peak can be clearly observed. We find that the position of the G peak for tBLG doesn't shift much compared with the monolayer graphene but the G' peak has a shift of ~25 cm^{-1}. The result agrees with reported experiments and calculations.

A similar result is found for flipped tBLG/hBN sample on Si/SiO_2 chips, but measurement for samples on Si/SiO_2 chip has several advantages. The sample on Si/SiO_2 chips has less noise compared to the stacks on PPC, and the step to subtract background signal is not needed. Also, the area of monolayer graphene and tBLG can be imaged with SEM for samples on Si/SiO_2 chips (Fig 3-8(b) inset), but for samples on PPC only optical images can be obtained and the identification of the monolayer and tBLG areas are not accurate. The possibility of performing multiple characterization methods on the same sample allows for a straightforward comparison. Although polymer residue and defects are found in the SEM image, modification of Raman spectra is not observed. This indicates Raman spectra is much less sensitive than SEM imaging in detecting defects.

In both type of samples, we don't observe R and R' peaks. The possible reason is that these peaks are weak at the twisted angle and laser energy in our experimental setup. But the measurement we performed show the possibility to integrate the Raman spectroscopy measurement into the procedures of device fabrication and other characterization method. Especially, measurement for flipped stacks on Si/SiO_2 chip give us the Raman spectroscopy with reasonably high resolution. With a further systematic measurement, a better understanding of Raman spectroscopy of tBLG is expected.

3.2 Scanning electron and Atomic force microscopy

In General, optical images of stacks can give a satisfactory solution for designing patterns and fabricating devices. However, bubbles formed during the pick- up procedure turns out to be the main roadblock in improving the quality of devices. The size of these defects is usually smaller than the resolution of optical microscope. To characterize and obtain better understanding of these defects, we employed atomic force microscopy (AFM) and scanning electron microscopy (SEM) to image our sample with a higher resolution.

3.2.1 scanning electron microscope

Getting the SEM image of the stack seems to be a straightforward task. However, there are some issues to confront to obtain clear images of the samples. The heterostructure that we are interested in are consisted of graphene or tBLG encapsulated between hBN. Such stacks can cause difficulty in SEM imaging because a conducting sample is required for SEM. Besides, the PPC used for picking up is hard to remove by dipping in acetone. Fig 3-8(a) shows an SEM image of a hBN/graphene/hBN stack made by the pick-up procedure. Due to the insulation of hBN and remaining PPC residue, the details of the graphene and bubbles in the stack can't be seen clearly. To overcome this, a furnace annealing step is needed before taking the SEM image. The image taken after performing the furnace annealing is shown in Fig 3-8(b). We find the resolution is largely improved after annealing. And to further improve the resolution of the underlying graphene, we use a lower voltage for SEM imaging. Rather than the 5kV that people usually used in SEM imaging, we find a voltage of 1~3 kV works better for imaging the encapsulated stacks.

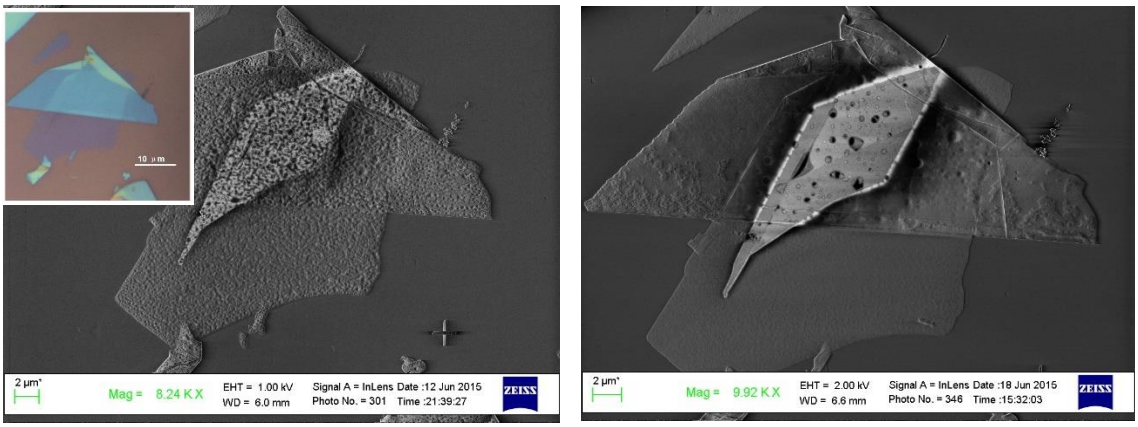

Fig 3-9 SEM images of hBN/graphene/hBN stack before (a) and after (b) furnace annealing (inset is optical image of the same stack)

In the SEM image, the underlaying graphene looks brighter compared with the hBN area. The location of bubbles can also be seen in the image. In Fig 3-9(b), we can identify the edge between monolayer and bilayer graphene because the top hBN we use for this stack is less than 10nm in thickness. The identification of layers becomes harder as the thickness of hBN increases. For hBN with thickness of 20~50 nm, the underlying graphene shows a bright profile but telling the edge of layers turns out to be hard. Meanwhile, bubbles in the stack can still be observed from the SEM image. Two more SEM images of the stack are shown in Fig 3-10 with the inset optical image.

3.2.2 SEM image of flipped stacks

In the pick-up procedure, we need to firstly pick up a layer of hBN as the substrate to pick up other layered materials by van der Waals force. The normal pick-up procedure will always leave graphene

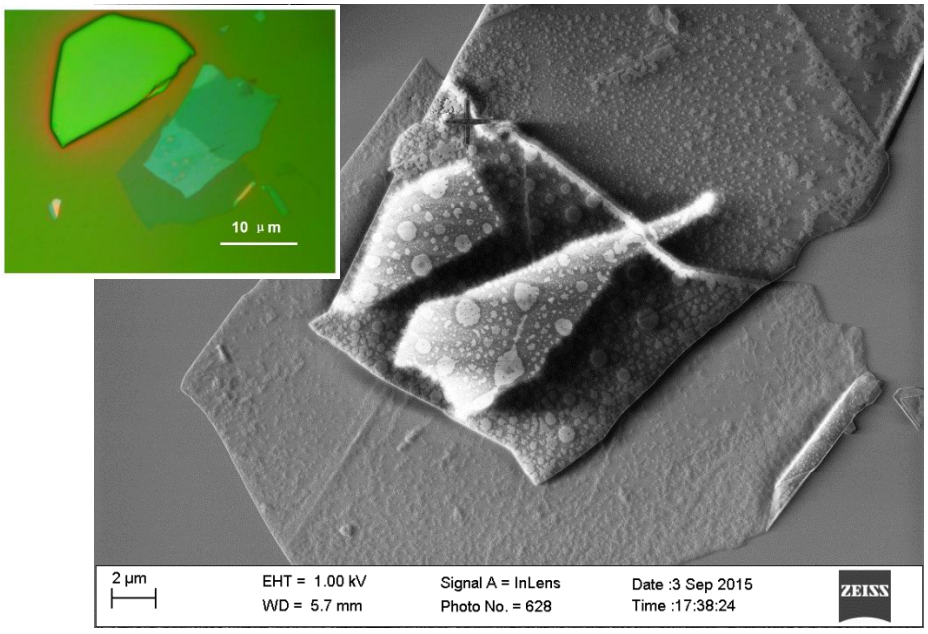

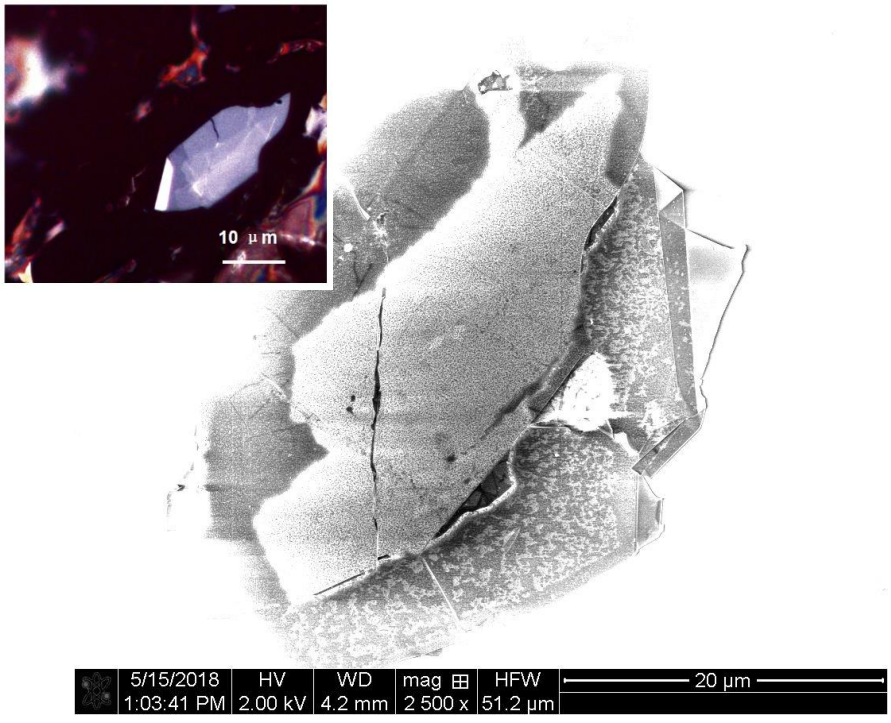

Fig 3-10 Additional SEM and optical images of stacks. Insets are optical images of the same stack on the Si/SiO_2 chip and PPC stamp respectively.

covered by the top hBN. A method of reversing the stacking order is proposed by Kim et al. [46]. The schematic diagram to reverse the stacking order using one water soluble polymer and another non water soluble polymer is shown in Fig 3-11. An alternative method is proposed by Zeng et al. [47], that the stack on the polymer is directly flipped and attached on the Si/SiO_2 chip and the polymer is then evaporated in furnace. In our experiment, we tried both methods to flip graphene onto top and both methods work good for taking SEM image.

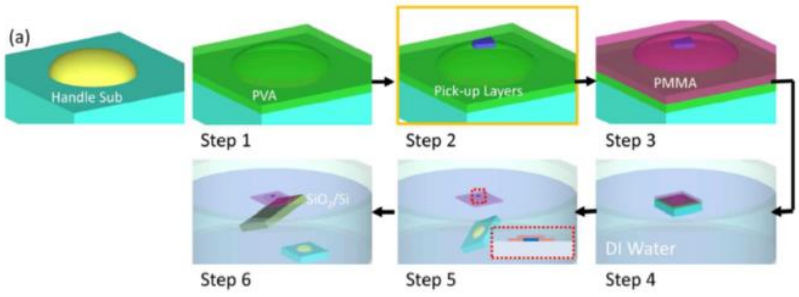

Fig 3-11 Schematic diagram of reversing the stacking order (adopted from [46]).

By flipping the stack, we are able to obtain high resolution images from the surface of graphene in the stack. This helps us to get a better understanding of the formation of defects in graphene and provides us with the guidance to improve the quality of devices. By examining these SEM images, we found a distinct difference between the stack made from graphene with and without pre-annealing (Fig 3-12). Previously, we showed that the Raman spectra of graphene before and after pre-annealing has different ratio between G and G' peak, indicating that there are modifications to the surface of graphene by furnace annealing. Here the SEM images give another proof that pre-annealing helps in reducing defects in the stack.

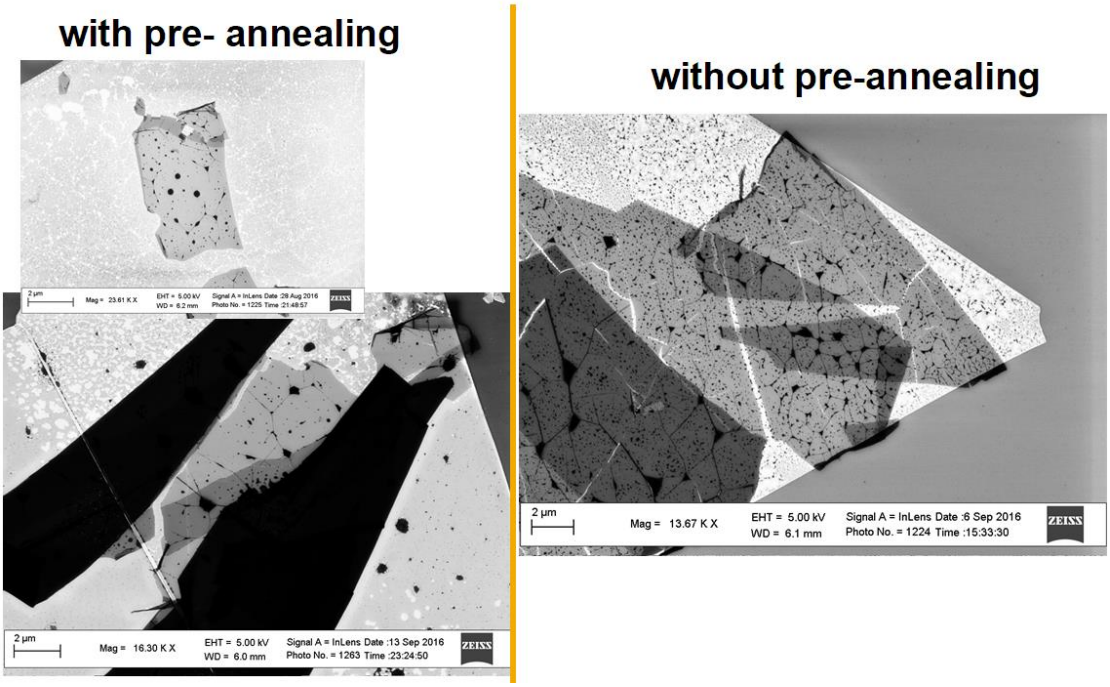

Fig 3-12 SEM images of graphene/hBN stacks made from graphene with and without pre-annealing.

The SEM images in Fig 3-12 also give us evidence that tape residue left on exfoliated graphene plays a role in the formation of "bubbles" in the stack. Besides the hydrocarbons from the atmosphere, tape residue is another source that induces defects into the stack. Pre-furnace annealing can effectively remove tape residue, so stacks made from graphene with pre-annealing have less defects. We also attempted furnace annealing after the stack in made, but it turns out to be much less effective comparing with the pre-annealing procedure. This agrees with the feature found from the SEM image. Defects in the stack are not individual "bubbles" but a network of point and line defects. So the "bubbles" are actually trapped between layers, making them hard to remove after the stack is made Fig (3-13).

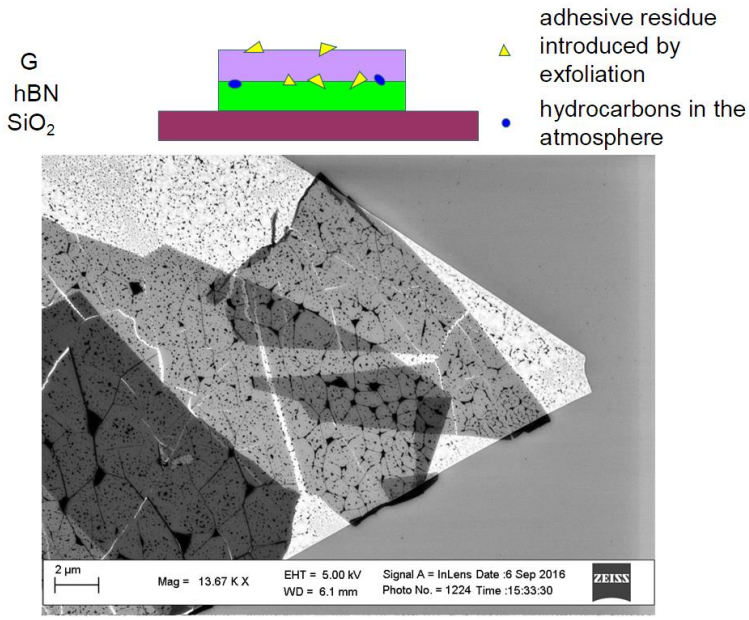

Fig 3-13 Illustration of "bubbles" in stack.

3.2.3 PeakForce tapping AFM

We also use AFM to image the surface of the stack. Fig 3-14 is the AFM images of graphene/hBN stack on PPC stamp. It shows similar features as the SEM images. AFM imaging provides more flexibility, image can be taken from soft substrates like PPC. No further treatment is needed so in principle AFM images can be taken between each step of the pick-up procedure. In our work, we usually take images of the exfoliated hBN on Si/SiO_2 chip to measure the thickness of flake and figure out the flat area that can be used for transfer (see section 2.1.1), and images of graphene/hBN stack to check the defects on graphene. AFM measurement has channels such as height, phase and height sensor. Here we show the image from phase channel, which gives good resolution of the defects. Different areas of the stack can be identified. There's an obvious step between hBN and graphene due to the abrupt change of mechanical properties at the edge while the edge of monolayer

graphene and tBLG is not always easy to identify. The fact that density of defects increases along with the slight step at the edge can be used to determine the area of monolayer graphene and tBLG.

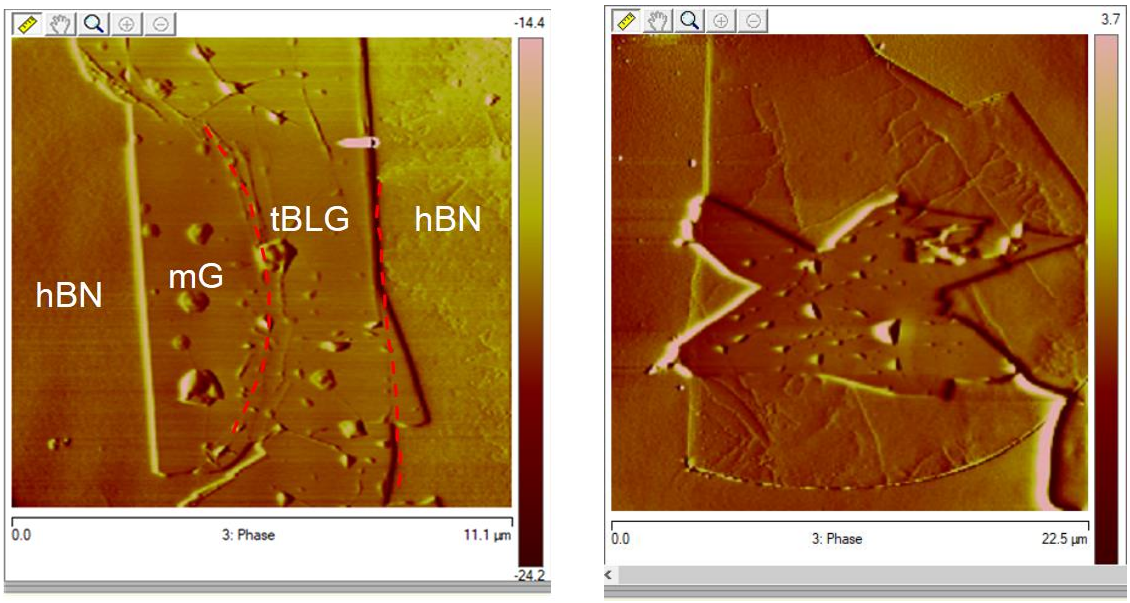

Fig 3-14 AFM images of graphene/hBN stack.

Another thing to mention is that for stacks used to take AFM images, we use "razor blade" graphene (see section 2.1.2) and the "tear-and-stack" method to make the tBLG heterostructures. SEM images of stacks made from graphene with and without pre-annealing provide evidence that tape residue plays a role in the formation of defects. To eliminate the effect from tape residue, we switch to "razor blade" graphene in our recent device fabrication. The AFM images and transport measurements (see next section) shows the device from "razor blade" graphene has less defects and high mobility in transport.

We also use the PeakForce tapping AFM [48] to improve the resolution of the image. The setup of PeakForce measurement is illustrated in Fig 3-15. At each spot of the sample, the measurement

of force vs z-position of the tip was performed. Related mechanical properties such as Young's modulus, adhesion and deformation can be calculated from the curve. The PeakForce mode performs better on soft substrates than the regular AFM, so it's very suitable for imaging the stacks on the PPC stamps.

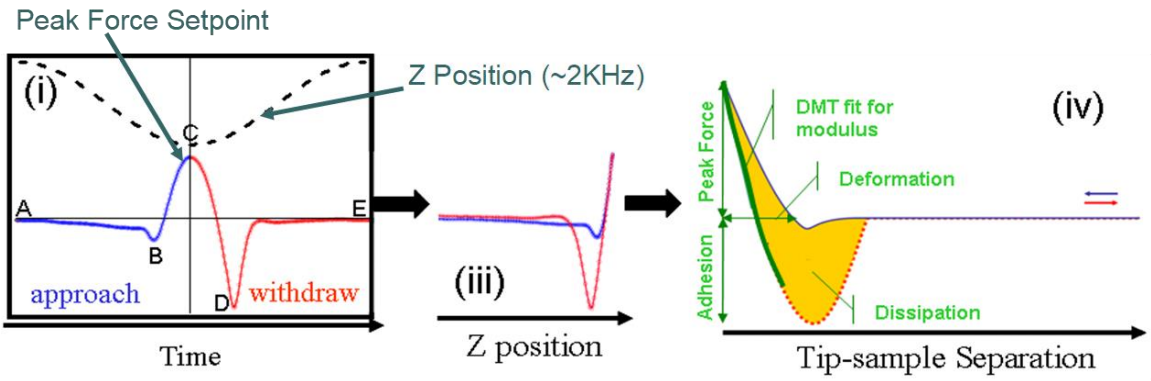

Fig 3-15 PeakForce tapping AFM (adopted from tutorial material provided with instrument).

Fig 3-16 is the image taken by PeakForce tapping AFM. The network of point and line defects are clearly seen in the image. And the density of defects at monolayer graphene and tBLG area are distinct. In the monolayer graphene part, a defect-free area of >10 μm in length can be found, but the area is limited to ~2 μm in length in tBLG part. In the "tear-and-stack" method, we need to align half of the graphene with hBN while the other half will contact the PPC polymer to tear the flake. We think this is associated with the difference in defect the two area because PPC residue may be deposited on the graphene in this procedure. Also, domains of different twisted angle can form in the stack [49], which may also induce defects in the tBLG area.

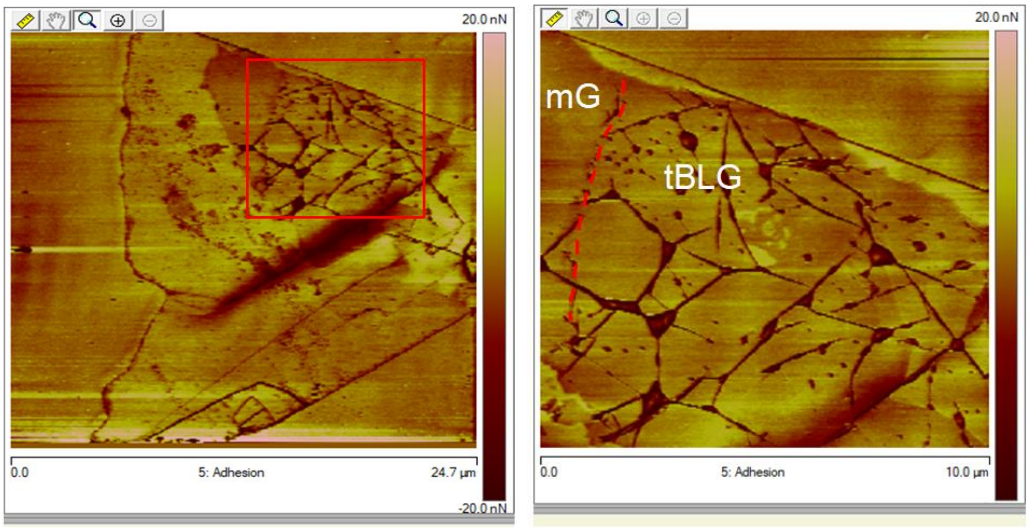

Fig 3-16 PeakForce AFM images of graphene/hBN stack on PPC.

To conclude, in this section we discussed our work on characterizing van der Waals heterostructures with SEM and AFM imaging. Analyzing these images gives some evidence about the formation of defects in the stack and hints on how to reduce the defects. And it also provides a guidance on designing the pattern to avoid defects in the device fabricated.

3.3 Transport measurements

Transport measurements are a widely used method to characterize properties of materials. After the stack of 2D materials is etched into a specific pattern (for example, a Hall bar), and contacted with metal electrodes, electric transport measurements can be performed to verify related properties of the device. Here a monolayer graphene Hall bar device is used to illustrate how to analyze the properties with experimental transport measurement data.

3.3.1 field effect mobility and Hall mobility

In transport measurements, mobility is used to characterize the response of electron to the applied electric field. In general, higher mobility is related to less scattering occurring in the material in electric transport. In 2D material devices, mobility is widely used as a reference of the quality of the device. Using the Drude model [13], conductivity σ of a material is related to mobility μ by a simple equation:

$$\sigma = n\, e\, \mu \tag{3-2}$$

where *n* is the carrier density and *e* is the value of elementary charge.

In Eq (3-2), the carrier density can't be directly measured, and depending on how the carrier density is deduced, a variety of definitions of mobility are given by the calculation from Eq (3-2). There can be difference in the value by using different definitions. In this section, we will show how the two commonly used definition of mobility, field effect mobility and Hall mobility, can be calculated from transport measurement data.

Transport data is taken from a monolayer graphene device encapsulated in hBN with the Si/SiO_2 working as the back gate. An optical image of the Hall bar device is shown is Fig 3-17(a). Carrier density can be tuned with the Si/SiO_2 back gate. When a bias voltage is applied on the device, the conductance will be observed varying with the carrier density thus with the gate voltage. A four-terminal measurement at 1.5K with zero magnetic field is shown in Fig 3-17(b) and the inset is the setup for the measurement.

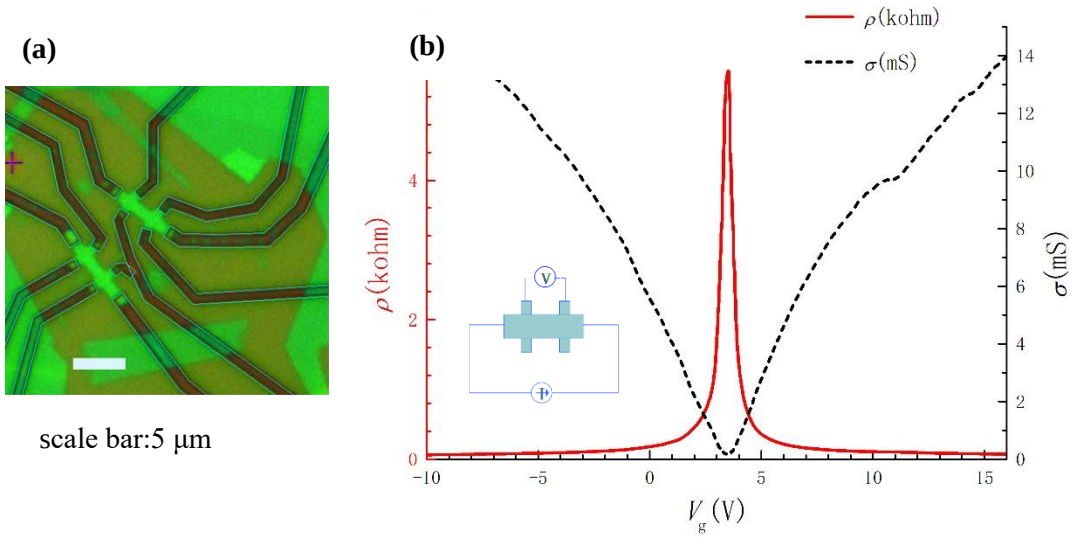

Fig 3-17 Field effect measurements. (a) optical image of the monolayer device. (b) conductivity and resistivity as a function of gate voltage.

with a model of parallel plate capacitor, carrier induced by gate voltage is given by,

$$n = \frac{\varepsilon\,\varepsilon_0}{t\,e} V_g \tag{3-3}$$

in the equation ε=3.9 and ε_0 = 8.85×10^{-12} F · m are the electric constant of SiO_2 and free space, respectively, t = 300 nm is the thickness of SiO_2 layer on the chip. Plugging these values into Eq (3-3) gives n = 0.072×10^{12} V_g cm^{-2}/V. Thus, we get the relation between carrier density and gate voltage, and plugging Eq (3-3) into Eq (3-2) gives us the so-called field effect mobility:

$$\mu = \frac{t\,\sigma}{\varepsilon\,\varepsilon_0 V_g} \tag{3-4}$$

In practice, $\frac{\sigma}{V_g}$ is usually replaced by $\frac{d\sigma}{dV_g}$ taken from the linear fit of σ vs V_g:

$$\mu = \frac{t}{\varepsilon\,\varepsilon_0}\,\frac{d\sigma}{dV_g} \tag{3-4'}$$

In the device shown here, the linear fit of σ vs V_g in Fig 3-17 has a slope of -1.65 mS/V and 1.75 mS/V for low carrier density on hole side and electron side respectively. This gives the field effect mobility of ~150,000 $cm^2 \cdot V^{-1} \cdot s^{-1}$. The value indicates our device has pretty high quality though the SiO_2 back gate is less effective in screening density inhomogeneities than the local graphite gates [50].

Carrier density can also be calculated from the classical Hall effect measurement. The measurement value of Hall coefficient R_H is given by

$$R_H = \frac{V_H}{I_b B} \tag{3-5a}$$

Where I_b is the biased current through the device, B is a weak magnetic field applied perpendicular to the device and V_H is the Hall voltage, or the transverse voltage in Hall effect.

R_H is related to the carrier density by

$$R_H = \frac{1}{n\,e} \tag{3-5b}$$

Fig 3-18 shows the plot of $1/R_H$ vs V_g measured at B = 0.15T. The slope from linear fit gives $n\,e$ = 0.106 V_g $T \cdot kohm^{-1} \cdot V^{-1}$, or n = 0.066 $\times 10^{12}$ V_g cm^{-2}/V. The value is close to the one from the model of a parallel plate capacitor in Eq (3-3), indicating most of the induced charges by back gate are free charges that contributes to the conduction of the device. In Hall effect measurement the conductivity σ can be measured at the same time. Using Eq (3-2), the Hall mobility μ_H is given by

$$\mu_H = \frac{R_H}{\sigma} \tag{3-6}$$

Fig 3-19 is the plot of calculated Hall mobility from Eq (3-6) as a function of gate voltage. We find the Hall mobility has a value of ~150,000 $cm^2 \cdot V^{-1} \cdot s^{-1}$ at low carrier density, which is close to the

field effect mobility previously calculated, and the value decreases to ~50,000 $cm^2 \cdot V^{-1} \cdot s^{-1}$ as the carrier density increases.

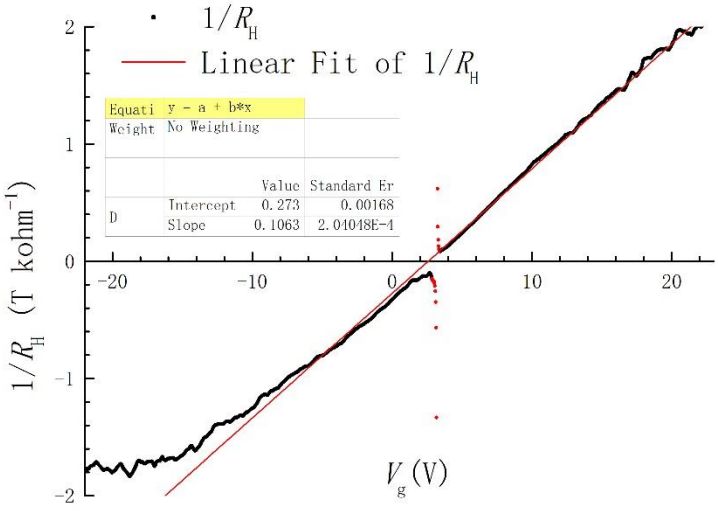

Fig 3-18 $1/R_H$ vs. V_g.

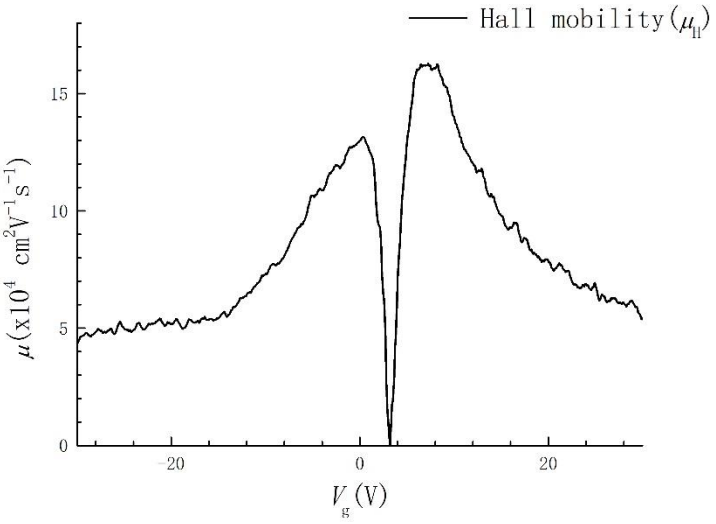

Fig 3-19 Hall mobility.

Another feature pointed out by people in transport measurements of monolayer graphene is that the maximum resistivity near the charge neutrality point (CNP) always fall into a small range near $h/4e^2 \approx 6.45$ kohm regardless of the mobility of the device [4, 51], and is believed to be related to the intrinsic property of electronic systems described by the Dirac equation. The feature is also verified on our device (Fig 3-17), with the maximum resistivity of ~5.7 khom. Though errors can come from the rough estimation of the aspect ratio of the device and a slow response on the quick change of resistivity when sweeping through CNP in the measurement. the measurement result has a good agreement with reported data.

3.3.2 magnetoconductance measurements

Magnetoconductance measurements are widely used to study the interaction of material with magnetic field. Here we perform measurement on the monolayer graphene device in perpendicular magnetic field. A map of longitudinal resistance as a function of gate voltage and magnetic field in shown in Fig 3-20. The features from such a measurement is referred as a "Landau fan". A simple explanation of a Landau fan is given here by considering Eq (1-22) in Chapter 1,

$$B = \frac{h}{e}\frac{D}{L^2} = \Phi_0 \, n/g \tag{1-22}$$

and the physics explanation behind it is that in each fully filled Landau level, one flux quanta goes through one cyclotron orbit.

And we already see in section 3.3.1 that the carrier density n is proportional to the gate voltage, that is $n = 0.072 \times 10^{12} V_g$ cm^{-2}/V. And in Landau fan diagram, multiple Landau levels are filled, so we need to sum up the degeneracy of each Landau level, so g in Eq (1-22) need to be replaced by $\sum g_i$ $(i = 0, 1, 2, \dots)$. As a result, when using the gate voltage and magnetic field as variables and plugging in the numerical results into Eq (1-22), the condition that Landau level is fully filled is given by the equation,

$$B(\mathrm{T}) = \frac{2.98}{\sum g_\nu} V_g(\mathrm{V}) \qquad (\nu = 0,1,2,\dots) \tag{3-7}$$

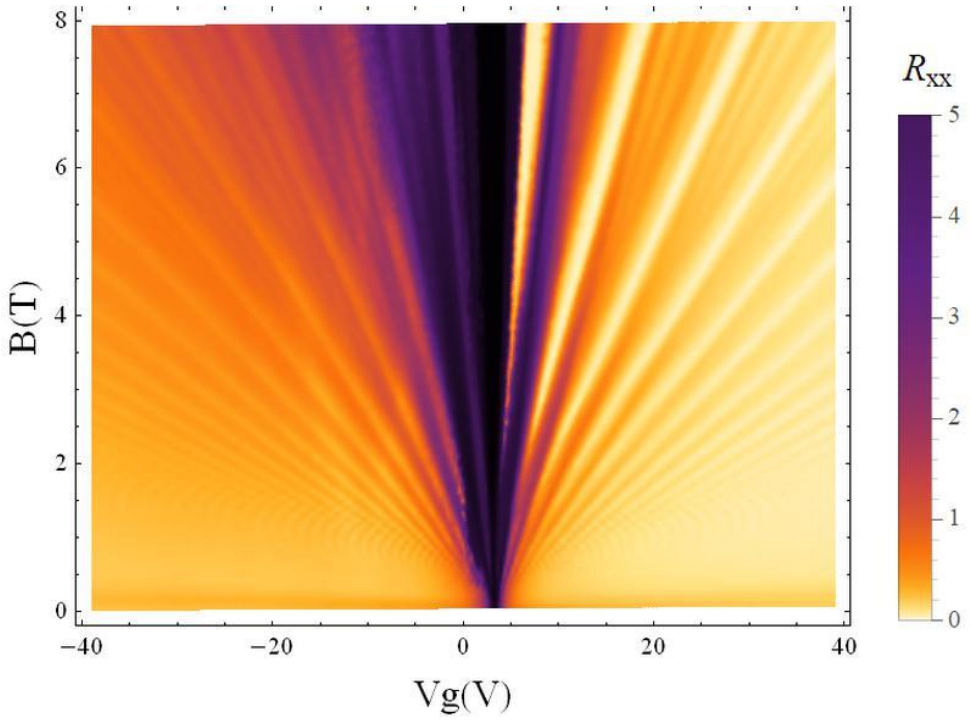

Fig 3-20 Landau fan diagram of R_{xx} for monolayer graphene.

When the condition Landau level being fully filled is satisfied, the longitudinal resistance in Shubnikov-de Haas oscillations (SdHOs) regime reaches minimum and turns to zero when system

evolves into quantum Hall regime. From Eq (3-7) we see that the minimum resistance should form a series of straight lines in the B-V_g map, which agrees with the experimental data shown in Fig 3-21.

To further check the magnetoconductance measurement quantitatively, the map of dR_{xx}/dV_g is plotted in Fig 3-22 to give a higher contrast on the oscillations in the Landau fan diagram. For monolayer graphene, the degeneracy of the lowest Landau level is g=2 while all higher Landau levels has a degeneracy of g=4 [6,18]. So, in the case of monolayer graphene, Eq (3-7) has the following form,

$$B = \frac{2.98}{4(\nu+\frac{1}{2})}V_g \qquad (\nu = 0,1,2,\dots) \tag{3-7'}$$

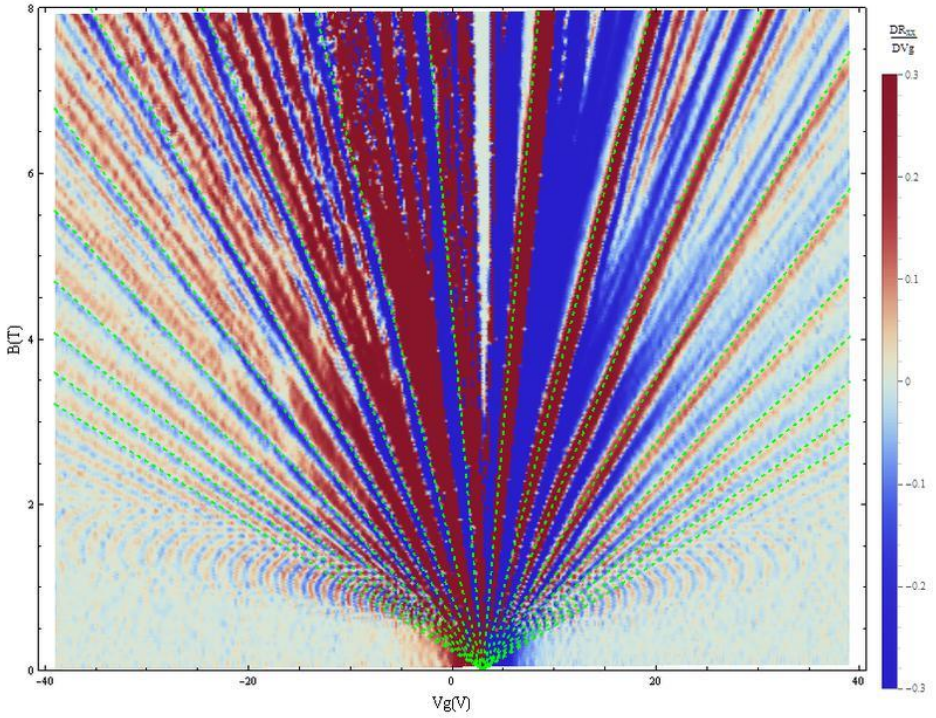

Fig 3-21 Landau fan diagram of dR_{xx}/dV_g for monolayer graphene.

In practice, the Landau fan diagram is fitted with the equation,

$$B = \frac{0.745}{(i+\frac{1}{2})}\alpha\,(V_g - V_D) \quad (i = 0,1,2,\ldots) \tag{3-7''}$$

the fitting result is shown in Fig 3-21 as the dashed green lines. The only parameters we adjust to fit experimental data are V_D, which is used to adjust the shift of V_g from CNP, and α, which gives a slight correction to the dependence of carrier density on V_g (all Landau levels are fitted with the same α. The value of V_D and α is obtained by manually adjust the fitted line until all the lines are aligned with the minimum of the resistance. We find that V_D = 3.0 V and α = 0.975 gives the best fit to the data. The fitted lines agree well with the Landau diagram up to i = 10.

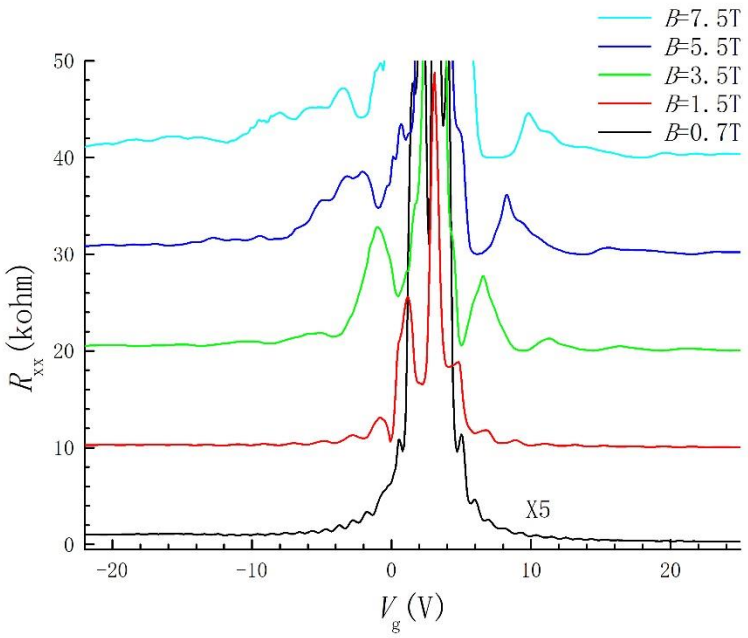

Fig 3-22 Line traces of R_{xx} vs V_g taken at different magnetic field (lines are vertically shifted by 10 khom).

We can make line traces along constant magnetic field in Landau fan diagram to take a closer look at the measurement result. The SdHOs arises at magnetic field lower than 0.4 T and in the line trace taken at B = 0.7 T in Fig 3-22, we can clearly observe the periodic oscillations, proving the device has a high mobility. On the electron side ($V_g > V_D$), R_{xx} decreases to zero at 3.5 T as evidence of quantization in the system. At higher magnetic field, the lift of the four-fold degeneracy in graphene is observed. In our device, carrier density is tuned by SiO_2 back gate and perpendicular electric field proportional to the gate voltage is also induced. The lift of the degeneracy can be explained by Zeeman splitting caused by the magnetic field.

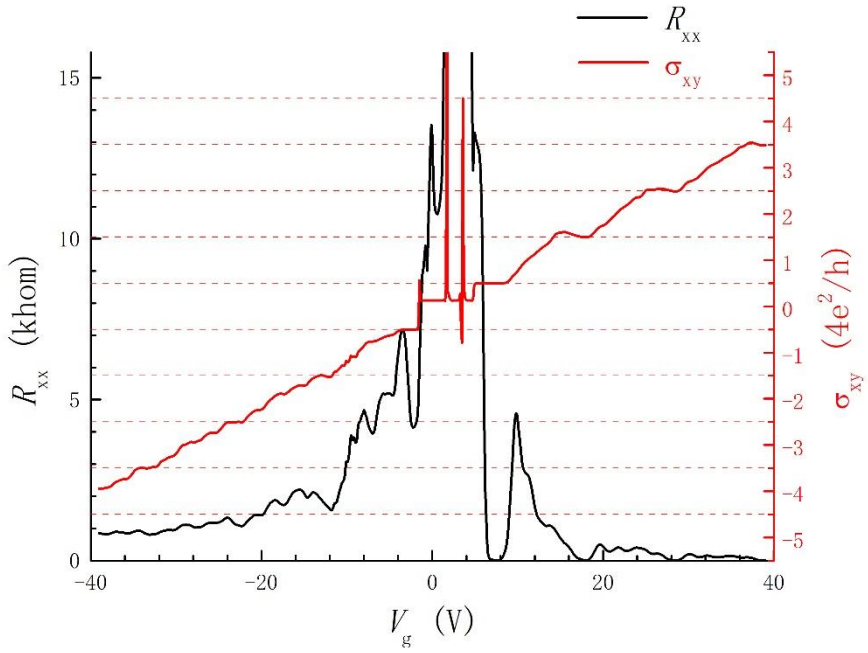

Fig 3-23 Line trace of R_{xx} and σ_{xy} vs. V_g at B = 7.5 T.

Fig 3-23 shows the line trace of R_{xx} and σ_{xy} at B = 7.5 T, which gives a clearer evidence of the Zeeman splitting. R_{xx} shows addition local minimum between Landau levels. On the hole side, the measured resistance has a finite value, and we think that's because the contact resistance is higher on hole side and the signal measured by lock-in is too weak when resistance on device is close to zero. And the measurement of transverse conductivity (σ_{xy}) indeed show plateaus on both electron and hole side. The quantization of the plateaus agrees with the theoretical value given by Eq (1-24). Also, at large gate voltage, three smaller plateaus are observed between the main Landau levels, which agrees with the lifting of four-fold degeneracy by Zeeman splitting.

Lastly, the fractional quantum Hall effect, which may require a higher magnetic field to onset, is not observed in our device. The "plateau" at σ_{xy} near zero is the fake signal when the resistance exceeds the maximum measured value of the instrument.

Chapter 4 Characterization of twisted bilayer graphene devices

4.1 Overview of twisted bilayer graphene

In section 1.1.4 and 1.1.5, we have seen that the crystal structure and band spectrum are altered by stacking two graphene sheets with a twist angle. An increasing number of theoretical and experimental works have appeared since a feasible strategy, “tear-and-stack” [25, 26], was proposed to precisely control the twist angle. And in recent work, a Mott-like insulating state and superconductivity were observed in tBLG [11, 12], leading to a new wave of interest in the field of 2D materials. The twist angle has become a new parameter to consider in modifying the properties of materials. Works to study the twist angle related effect on other materials is also accumulating [52-54]. The following is a brief overview of the progress in tBLG devices from experimental aspect.

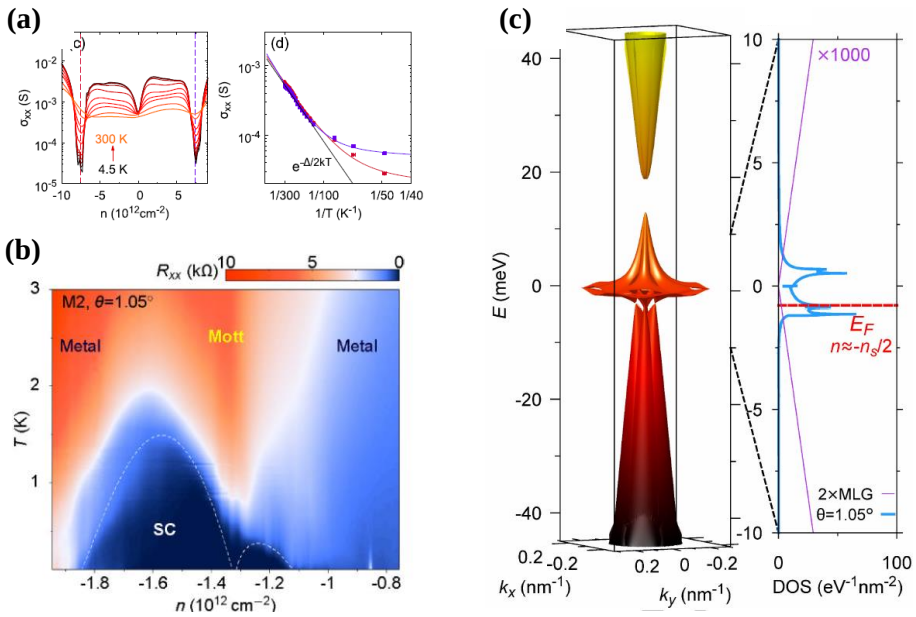

Fig 4-1 Overview of tBLG devices (a) the superlattice gap at full-filling [25]. (b) correlated Mott-like insulating state and superconducting state [12]. (c) band structure and density of states calculated with single-particle picture for twist angle of 1.05° [12].

The twisted bilayer graphene is one of the simplest structures for twisted 2D materials. Early experimental works of tBLG on Si/SiO_2 can be found in [55, 56]. In more recent works, the superlattice induced gap is reported on hBN encapsulated tBLG devices with small twisted angle (Fig 4-1(a)). The size of the reported gap varies in a wide range of 10 to 60 meV[11,25, 26, 57, 58], while the calculations shows the gap of ~10meV or less [59, 60]. This gap is induced at the carrier density of four electrons per moiré unit cell (full-filling), and we will refer it as the "superlattice gap". Later, the more surprising findings is reported in tBLG devices with a twisted angle of 1.1 degree [11, 12] (Fig 4-1(b)). Such angle has been predicted to be the "magic angle", where the low energy bands are flat and the Fermi velocity at Dirac points tends to zero [8]. However, the non-interacting picture fails to explain the observed Mott-like gap and superconductivity at carrier density near two electrons per moiré unit cell (half-filling). This indicates the Coulomb interaction

between electrons need to be considered in tBLG near magic angle. The strong correlations in the system are supported by the calculation of density of states (DOS), showing the energy scale is 3 orders of magnitudes smaller than that of two uncoupled monolayer graphene (Fig 4-1(c)). To tune the correlation features of tBLG, the interlayer spacing can be manipulated with hydrostatic pressure [61]. The correlated insulating and superconducting phases are induced in a device with twist angle of 1.27° (Fig 4-2), larger than the magic angle, under 2.21GPa, providing another degree of freedom to play with in tBLG.

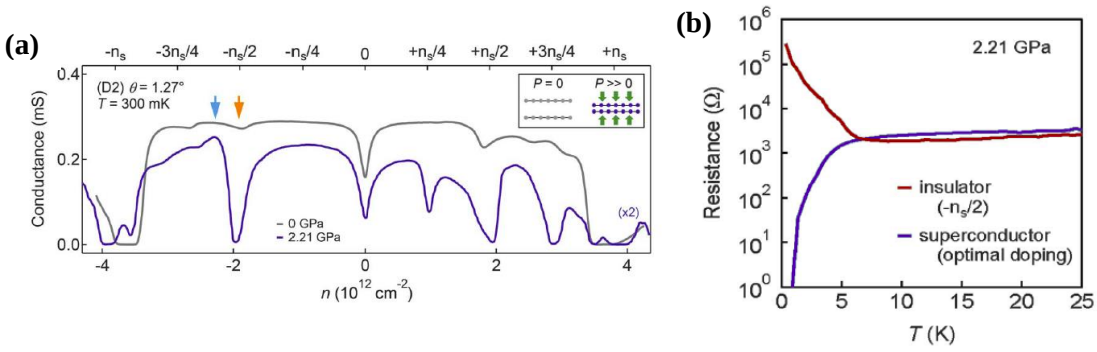

Fig 4-2 Correlated states in tBLG induced by hydrostatic pressure.

Works on tBLG won't stop here, experiments on many other aspects are still needed to resolve debates and understand this system better. Theoretical works also need more data from experiment to explain the insulating state and superconductivity in the system.

4.2 Measurement on device d151

4.2.1 field effect transport measurement

Optical image of a tBLG device (d151) made by the tear-and-stack method is shown in Fig 4-3(a). Patterns are etched into three different area and contacted with Cr/Au electrons. Measurements

mainly focus on the Hall bar pattern high-lighted by the red box in the image. Additional measurement results can be found in Supplementary Data part. Fig 4-3(b) is the four-terminal measurement of longitudinal resistance (R_{xx}) measured at T = 1.5 K and B = 0 T. Si/SiO_2 back gate is used to tune the carrier density in device. The charge neutrality point (CNP) shows up at V_g = 2.5 V. Two more peaks are found at V_g = -56.6 V and V_g = 60.0V, locates almost symmetrically to the CNP. These two peaks are related to the superlattice gap in tBLG. The twist angle is aimed at 1.1° in experiment, while the angle calculated from the superlattice gap turn out to be 1.35 ° (see the following text for detailed calculation). A few more devices are made, showing the actual twiste angle seems to be slightly larger than the aimed one. But currently the number of devices is too limited to confirm such a trend.

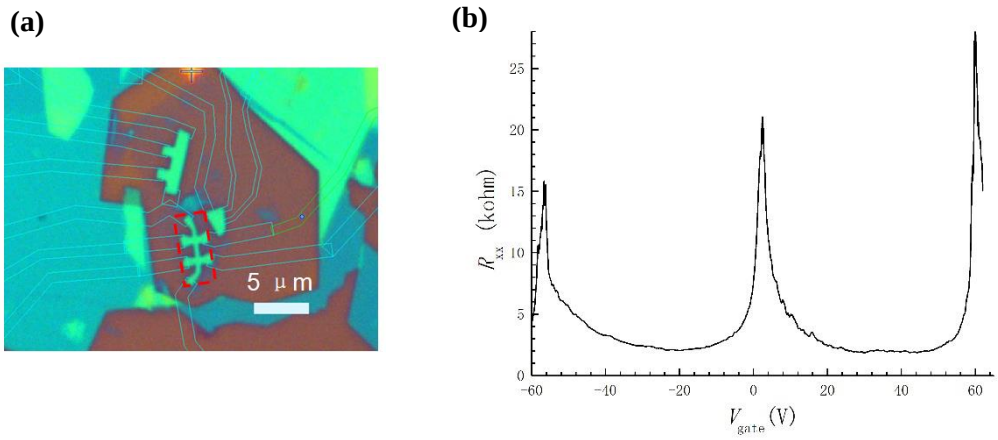

Fig 4-3 tBLG device d151 (a) optical image (b) resistance vs. gate voltage.

A similar analysis as in section 3.3.1 can be carried out here. The field effect mobility is calculated to be ~15,000 $cm^2 \cdot V^{-1} \cdot s^{-1}$, about 10 times smaller than the monolayer graphene device. We noticed the reduction of mobility is also observed in works mentioned above [8, 25]. We attribute the lower mobility to the increased density of defects in the stack and the flat band feature of tBLG. As we increase the carrier density, the resistance begins to saturate for $|V_g| > 20$ V but we don't see

evidence of correlated states near half-filling. This agrees with the reported works that the correlated states are only found near the magic angle. When the carrier density is further increased, resistance starts to increase, and the voltage where the superlattice gap shows up corresponds to the carrier density of $n_s = \pm 4.2 \times 10^{12}$ cm^{-2}. Because the superlattice gap is at four electron per moiré unit cell, the area of the moiré cell can be calculated and thus the twisted angle. The moiré wavelength is given by

$$\lambda = \frac{a}{2\sin(\theta/2)} \approx \frac{a}{\theta} \tag{4-1}$$

and n_s is related to the twisted angle by

$$n_s = \frac{4}{\frac{\sqrt{3}}{2}\lambda^2} \approx \frac{8\theta^2}{\sqrt{3}a^2} \tag{4-2}$$

From Eq (4-2), $n_s = \pm 4.2 \times 10^{12}$ cm^{-2} corresponds to the twisted angle of ~1.35°.

Asymmetric behavior is observed between electron and hole side. Since the contact resistance has little influence on the four-terminal measurement used in our experiment, we hypothesize that the asymmetric behavior is related to the band structure of tBLG, but more theoretical efforts are needed to understand this feature.

4.2.2 magnetoconductance measurements

Measurements are also performed on the device placed in perpendicular magnetic field. The map of longitudinal and transverse resistance vs gate voltage and magnetic field is shown in Fig 4-4 and 4-5. Series of Landau fans can be seen from the map. In the map of R_{xx}, fan diagram can be overserved originating from the CNP and the superlattice gap for $V_g > 0$ V. For $V_g < 0$ V, instead of the Landau fan feature, a high resistive area is observed for carrier density larger than the half-filling of moiré cell. For $V_g > 0$ V, Landau levels from the CNP and superlattice gap meet near the carrier density of half filling, where a lifting up of resistance is observed.

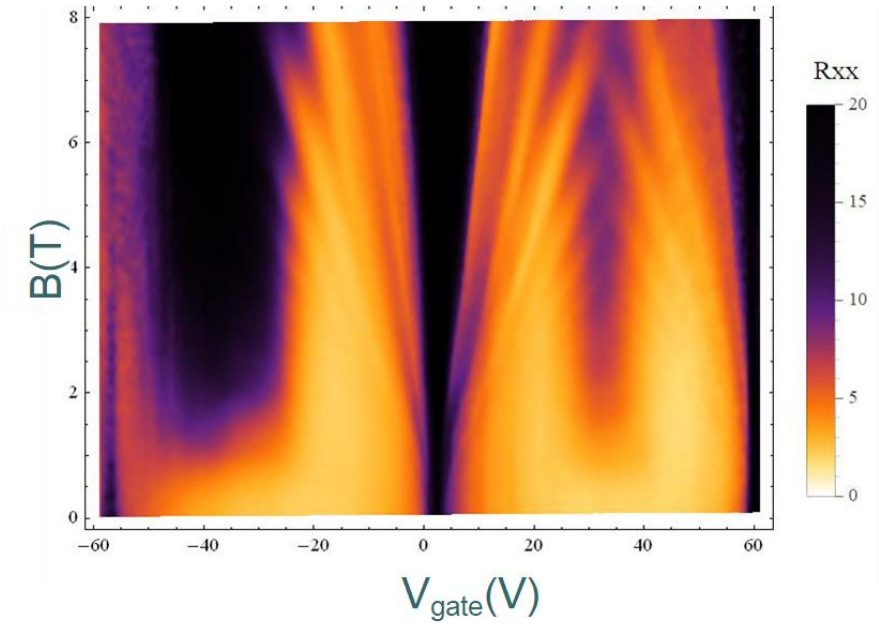

Fig 4-4 Landau fan diagram of R_{xx} for d151.

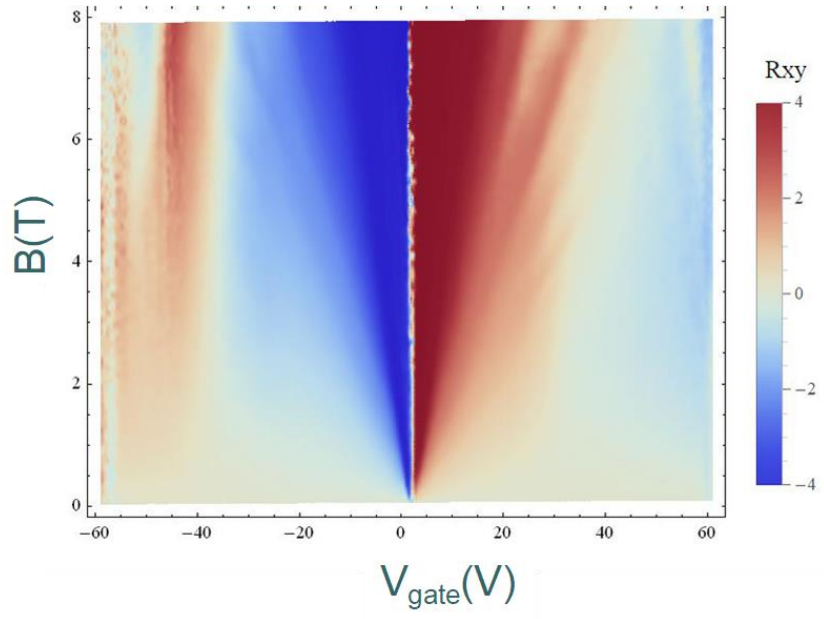

Fig 4-5 Landau fan diagram of R_{xy} for d151.

In the map of R_{xy}, the fan diagram at the CNP can be observed, but features from superlattice gap are note well defined. Near half-filling the change in sign of R_{xy} is observed on both sides, indicates the switch of carrier type there. This finding supports the statement that the peaks at $n_s = \pm 4.2 \times 10^{12}$ cm^{-2} comes from the superlattice induced gap, with the superlattice mini-band being half filled near the midway.

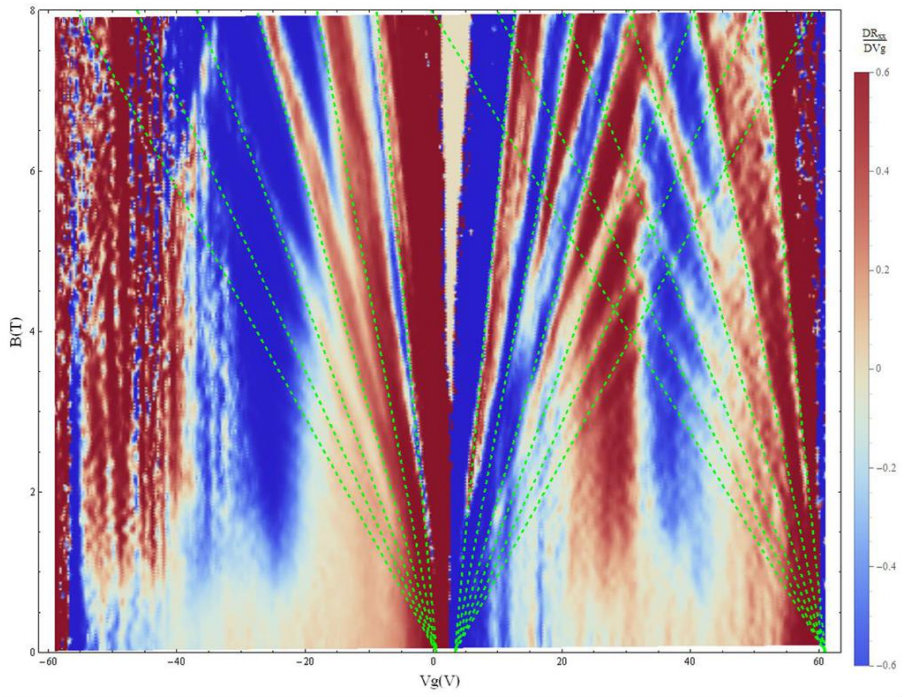

Fig 4-6 Landau fan diagram of dR_{xx}/dV_g for d151.

To bring up the Landau fan diagram with a clearer look, the map of dR_{xx}/dV_g is plotted in Fig 4-6 to help make a further analysis of the magnetoconductance data. We map the Landau fan diagram with lines of integer filling factors. Green dashed lines in Fig 4-6 shows the best fit to the experimental data. The carrier density is estimated using the parallel plate capacitor model with a correction factor being manually adjusted within 10% to fit with experimental data (see section

3.3.2 for detail). Theoretical investigations imply the filling factors for Landau fans from the CNP in tBLG should be in the sequence of monolayer graphene multiplied by two, that is, $\nu = \pm 4, \pm 12, \pm 20, \ldots$ corresponding to an eight-fold degeneracy. However, in our fitting the minimum resistance aligns with filling factors of $\nu = \pm 4, \pm 8, \pm 12, \pm 16, \ldots$. Similar results are reported in other works [12, 61]. Additionally, measurement results reported in [57] point out that Landau fans for $\nu = \pm 8, \pm 16, \ldots$ are fainter, indicating they result from the splitting of eight-fold degeneracy. In our data, we didn't see a clear difference in between $\nu = \pm 4, \pm 12, \pm 20, \ldots$ and $\nu = \pm 8, \pm 16, \ldots$ This suggests that the system has four-fold degeneracy in our device, similar to the case of AB stacked bilayer graphene. However, devices with lower disorder may give more information about the coupling in tBLG. We also notice that to give the best fit to the Landau fan diagram, the fitted lines for the electron and hole side do not intersect at B = 0 T, but leave a small gap at the CNP. This indicates the existence of charge paddles in our device and the possibility to further improve the device quality.

Landau fans from the superlattice gap at $V_g > 0$ V are also fitted in the same manner. There are hints that Landau fans also originate from the superlattice gap at $V_g < 0$ V. But because there's a large resistive area it's difficult to the data. Landau fans from the CNP and superlattice gap meet near the half-filling, but no evidence of crossing of Landau levels is observe. The Landau fan diagram also shows the longitudinal resistance near half-filling increases in high magnetic field, which is possibly related to the strong correlations in the system. But the resistive state at high carrier density in $V_g < 0$ V area and the asymmetry between electron and hole side of the systems remain to be a puzzle.

4.2.3 temperature dependence measurement

We also performed a temperature dependence measurement on device d161. Two rounds of measurement were performed and plotted in Fig 4-7. In the first measurement, we took line traces of longitudinal resistance vs gate voltage from varies temperature from 1.52 K to 150 K. A more careful investigation on temperature dependence was performed in the second measurement, and the line traces are converted into two-dimensional map as shown in Fig 4-7(b). The two rounds of measurement show similar features, indicating the result is repeatable.

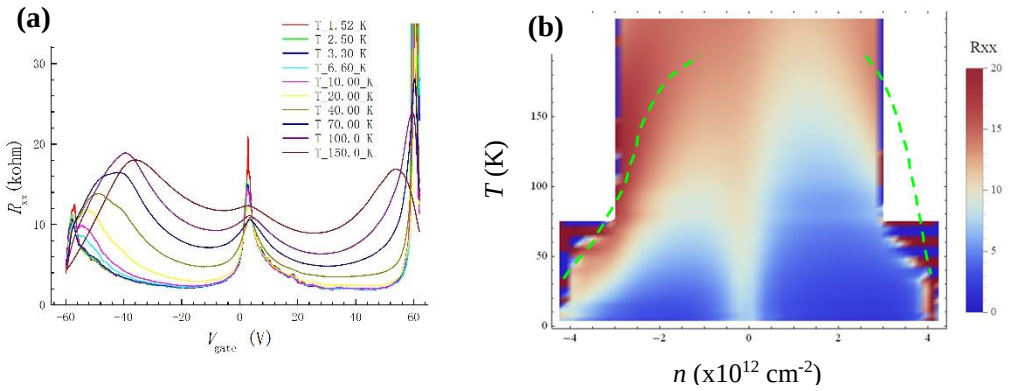

Fig 4-7 Temperature dependence measurement on d151.

A strong dependence of resistance on temperature is observed from the measurement. In Fig 4-7 (a), the line traces are well separated though we don't add any vertical shift between different temperatures. Another clear feature is that the local maximum of resistance at high carrier density is found to move towards the CNP as the temperature increases. Following the work in [62], we manually divide the 2D map (Fig-b) along the maximum resistance at high carrier density. Although the second measurement doesn't cover the local maximum in full range to avoid breakdown of the back gate, the division can still be estimated from the dome-like shape of

resistance in the 2D map. Both measurements show a clear trend that the local maximum is moving inwards, a discussion on this is given in the next section.

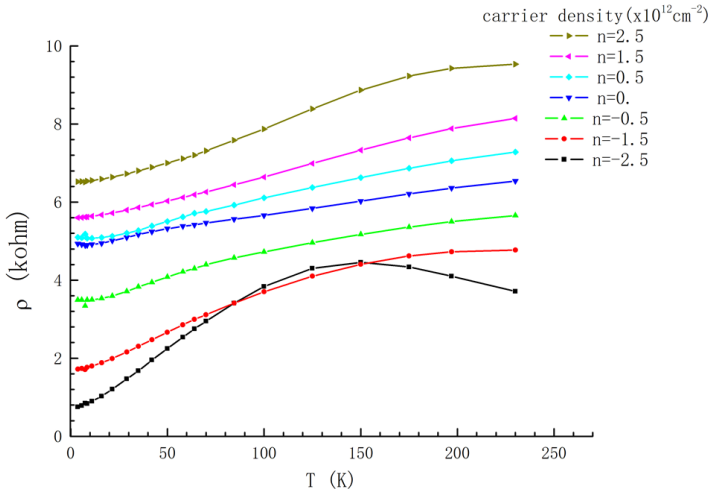

Fig 4-8 Temperature dependence for carrier density from -2 to 2×10^{12} cm^{-2}.

In Fig 4-8 and 4-9, we take line traces of resistivity along different carrier densities. The resistivity is obtained by simply multiplying the measured resistance by the aspect ratio of the device. In Fig 4-8, we check resistivity vs temperature over a wide range of carrier density, and lines are shifted vertically by 1kohm. A consistent trend of increasing in resistivity with temperature is observed for all measured carrier densities. The temperature of saturation or turning down is also observed to be carrier density dependent, which related to the inwards shifting of the local maximum in resistance. Also, the resistivity seems to change faster for higher carrier density, and a quantitative analysis will be given in the following text.

In Fig 4-9, we show the temperature dependence of resistivity of a small range near the carrier density of $n = \pm 2\times10^{12}$ cm^{-2}. No vertical shift is added between lines to illustrate the weak

dependence feature of resistivity on the carrier density. We find the line traces almost overlap with each other at T < 50 K for $n < 0$ and at T < 100 K for $n > 0$. The lines start to separate at higher temperature and the saturation of resistivity is observed round the same temperature.

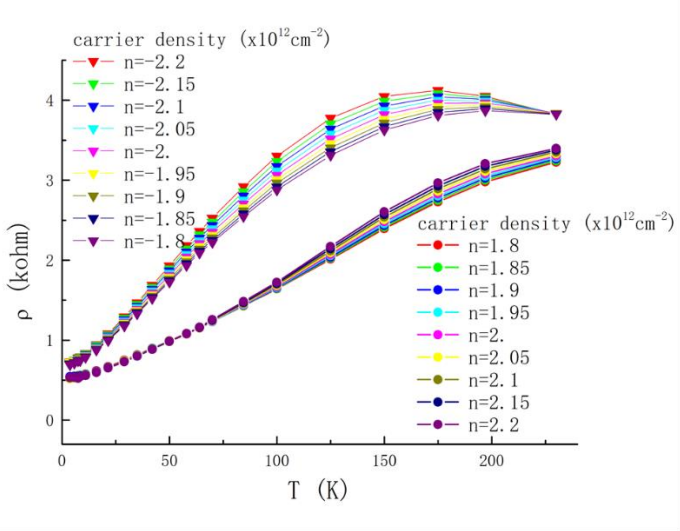

Fig 4-9 Temperature dependence near $n = \pm 2\times 10^{12}$ cm^{-2}.

Line traces in Fig 4-9 and Fig 4-9 gives us an overview of the temperature dependence of resistivity. For wide range of carrier density, the resistivity increases with temperature. And there's also a slow variation with carrier density that the resistance changes faster with higher carrier density. Besides, the asymmetry between A more detailed analysis of these features will be given in the following sections.

4.3 Additional measurement results from device d092

We also perform measurements on another device d092. Using Eq (4-2), the twist angle is calculated to be ~1.50°. The temperature dependence data shows similar features as device d151 illustrated in previous text. Fig 4-15 to 4-17 show the measurement results. Further analysis is still in preparation.

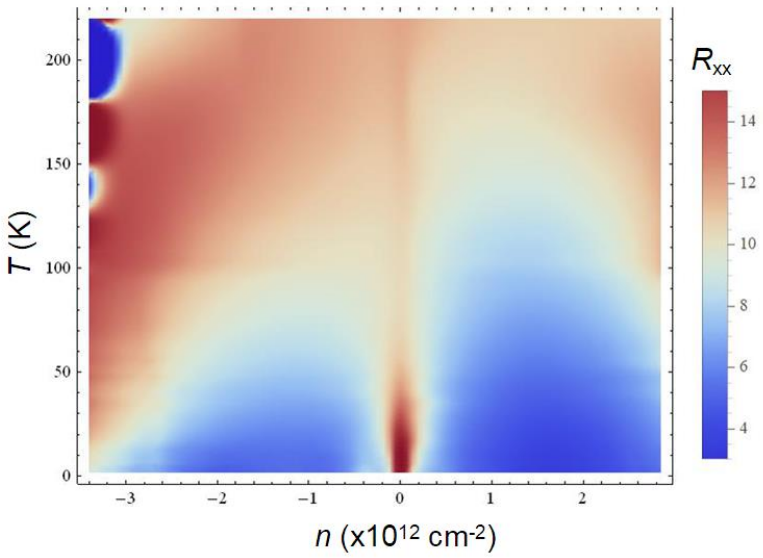

Fig 4-10 2D map of Resistance as a function of carrier density and temperature.

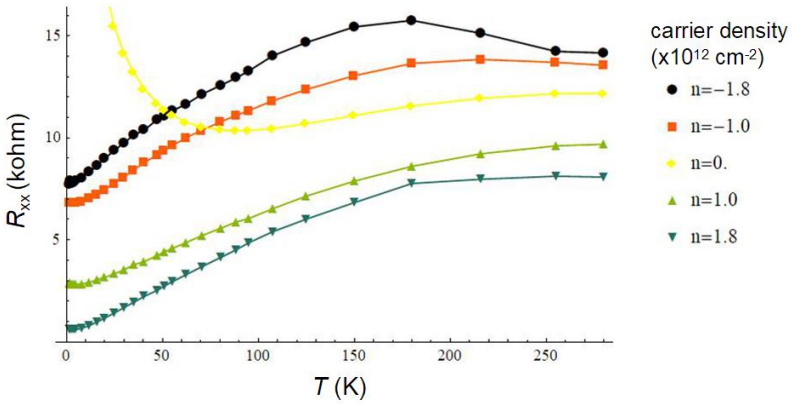

Fig 4-11 Temperature dependence for carrier density from -1.8 to 1.8×10^{12} cm^{-2}

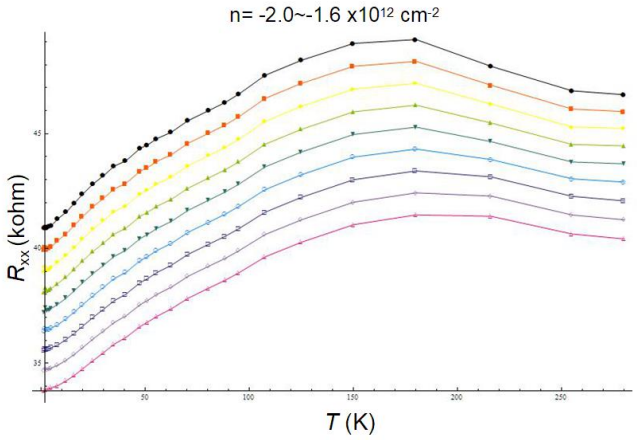

Fig 4-12 Temperature dependence for carrier density from -2.0 (black) to -1.6 (purple)×10^{12} cm^{-2}

4.4 Analysis of temperature dependence data on device d151

To understand the features in the temperature dependence measurement, we first investigate several related works from different groups. Temperature dependence of resistivity for a tBLG device with

twist angle of ~2° is reported in [58], and the temperature dependence is attributed to phonon scattering and the data is fitted by $\Delta\rho(T) = \alpha T^{\beta}$. The power index β ranges from 0.9 to 1.7 and

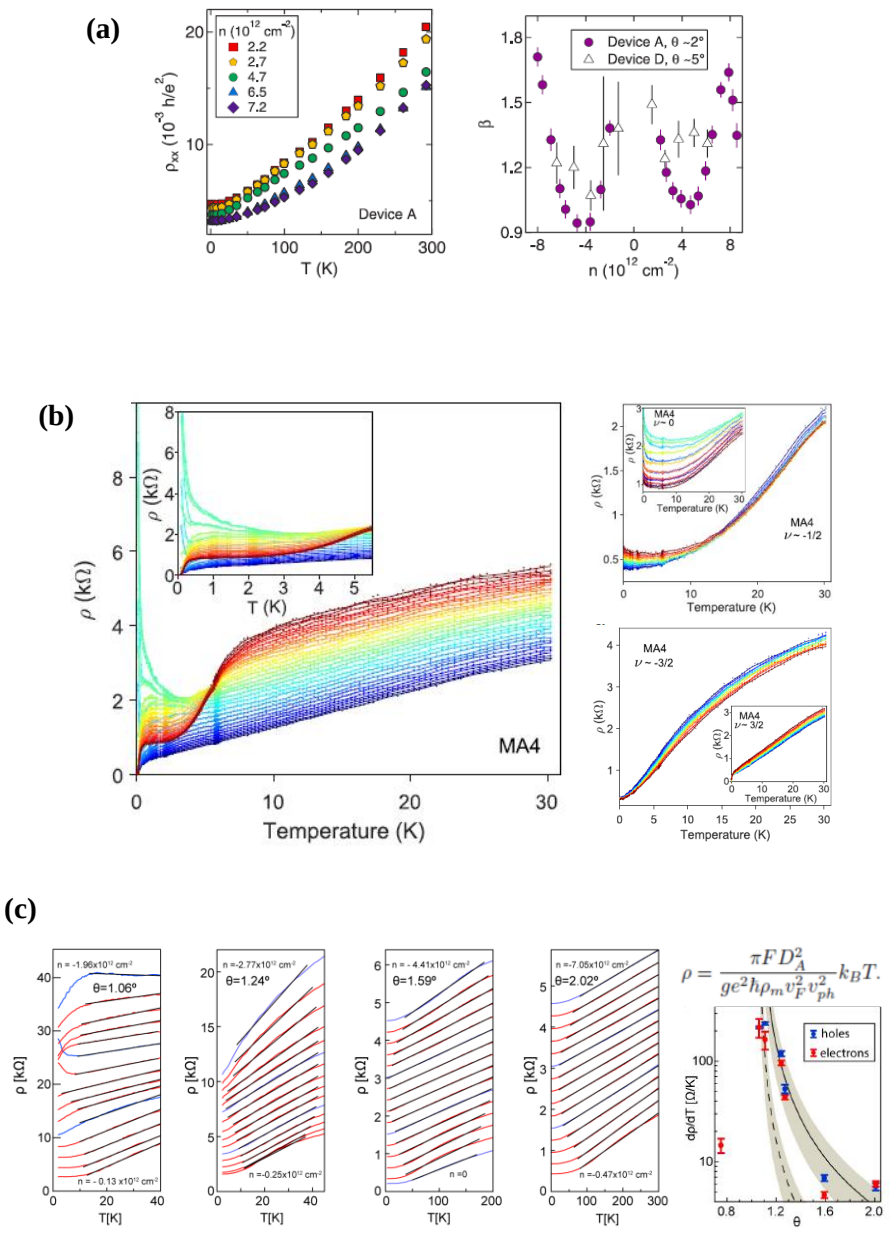

Fig 4-13 Overview of temperature dependence measurements on tBLG.

displays a W-shaped curve. Minimum locates near the half-filling with β = 0.9 and maximum appears as the carrier density approaches full-filling β = 1.6~ 1.7(Fig 4-13(a)). Recent works focus on the *T*-linear dependence of resistance at various twisted angle including the magic angle [62, 63]. The scattering rate extracted from the *T*-linear resistivity regime is in the same magnitude of $k_B/\hbar$, which is a hallmark of strongly correlated systems [63] (Fig 4-13(b)). And the *T*-linear response over a wide range of temperatures for twisted angles varying from 0.75° to 2° is reported in [62]. The value of dρ/dT extracted from the linear fit for the same twisted at different carrier density is nearly a constant. And dρ/dT vs twisted angle agrees well with the theoretical prediction of phonon induced scattering [64]. Another work that worth mentioning explains the excess resistivity in monolayer graphene/hBN superlattice [65]. Theoretical investigation shows that the asymmetry resistivity on electron and hole side is caused by the umklapp electron-electron scattering (Fig 4-14).

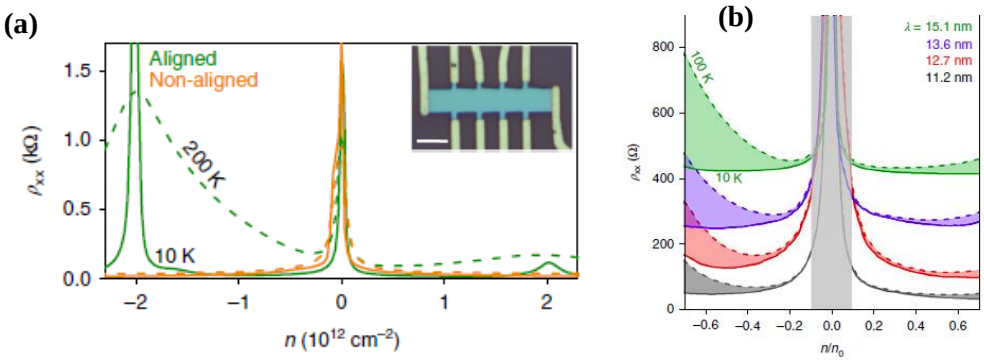

Fig 4-14 Excess resistivity caused by umklapp electron-electron scattering in monolayer graphene/hBN superlattice.

4.4.1 fitting of the temperature dependence data

Works above unveiled some of the truth in the mechanism of temperature dependence of resistivity in tBLG and give us some guidance on analyzing data from our devices. But there are also a few

different features found in our measurement that can be helpful for a better understanding of the transport properties of tBLG.

First, we introduce the mean-free-path model to show that the features in temperature dependence measurement is related to the moiré pattern in tBLG. The relation of conductivity σ and mean free path l is given by

$$\sigma = \frac{2e^2}{h}\sqrt{\pi n}\cdot l \tag{4-3}$$

where n is the carrier density. Using the moiré wavelength given by Eq (4-1) as the character mean free path, we plot the character resistance ($1/\sigma$ multiplying the aspect ratio of the device) as a function of gate voltage in Fig 4-15(a) in comparison with the temperature dependence result. We find that the measured resistance keeps below the character resistance except for the carrier density near superlattice gap at low temperature. We can conclude that the mean free path of electron and hole are longer than the moiré lattice, so the scattering induced by the superlattice should be taken into account to explain experimental data. And interestingly, the saturation of maximum resistance is in the same range as the character resistance. The finding proves that the features in intermediate temperature is related to the moiré superlattice in tBLG, and the maximum resistance may also relate to the scattering from superlattice.

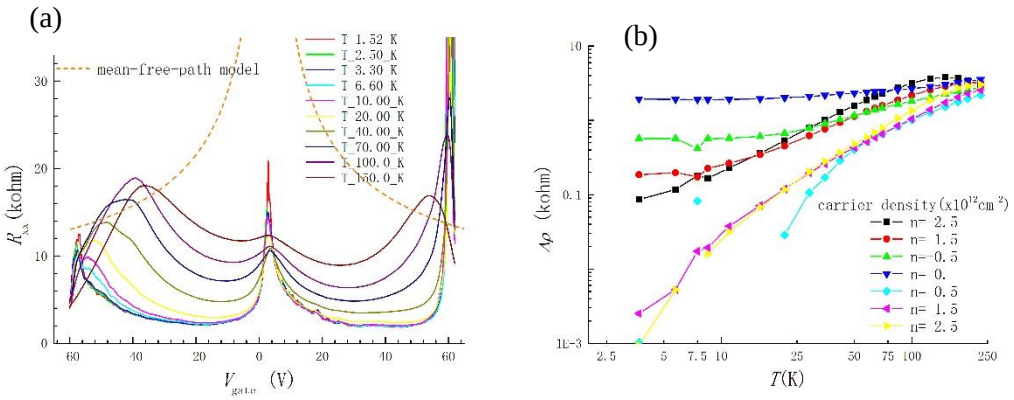

Fig 4-15 Analysis of temperature dependence measurements on d151.

We also re-plot Fig 4-8 as $\Delta\rho$ vs T in log-log coordinate. Traces should show up as straight lines with slope of 1 if $\Delta\rho$ follows T-linear dependence. However, it turns out in the plot that the slope varies with carrier density. The deviation from the T-linear dependence agrees with the original data plotted in Fig 4-8. On the other hand, it can be seen that $\Delta\rho$ follows straight lines in a wide range of temperature, so the power law dependence on T is still satisfied by the resistivity.

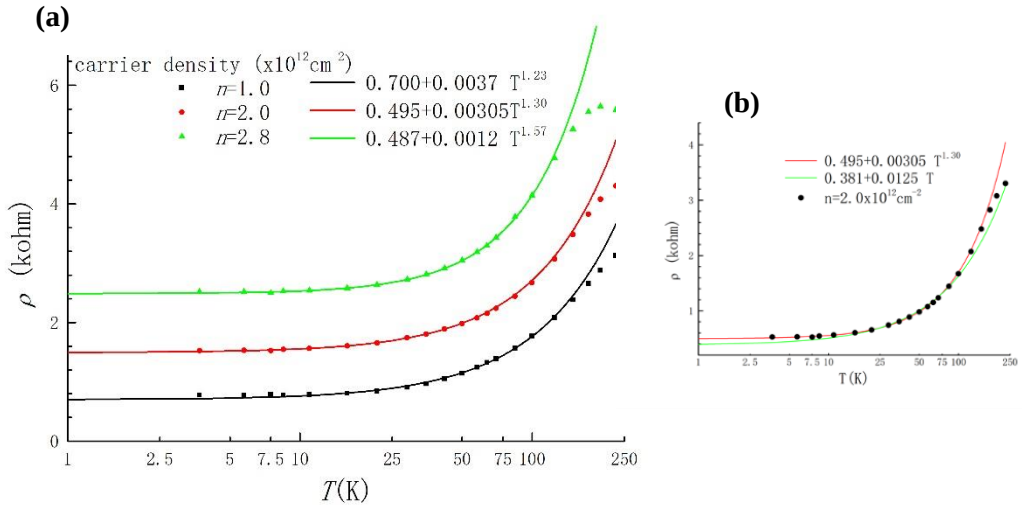

Fig 4-16 Resistivity vs T at different carrier density fitted by Eq (4-4).

Analyses above indicates our measurement result follows the power law in temperature dependence, similar to the work reported in [58]. However, fitting the data with $\Delta\rho(T) = \alpha T^{\beta}$ can be tricky because the resistivity is also affected by factors like disorder and localization at low temperature regime, so the value of $\rho(0)$ can't be directly extracted from the experimental data. To overcome this, we add a term ρ_0 accounting for the residue resistivity and use the equation

$$\rho(T) = \rho_0 + \alpha T^{\beta} \tag{4-4}$$

to fit the temperature data. The result is plotted in Fig 4-13(a). And in comparison, linear fit is shown in Fig 4-16(b) for carrier density of $n = 2\times10^{12}$ cm^{-2}. In both the linear fit and power law fit, the fitting range is manually adjusted to make the fitting cover the largest temperature range. We find the power law given by Eq (4-4) agrees well with data in a wider temperature range while the linear fit deviates from measurement for $T < 10$ K. This verifies that the temperature dependence of tBLG is phenomenologically better described by the power law, but it doesn't exclude the possibility that T-linear dependence is still valid in explaining the mechanism of excess resistivity (see discussion in next section). But here we will focus only on the power law fitting to quantitatively describe the system. Fig 4-16(a) shows fitting for three different carrier densities on electron side, and parameters that give the best fit are show in the legend of the plot. The power indexes βvary from 1.23 to 1.57 and the residual resistivity ρ_0 decreases from 0.70 kohm to 0.49 kohm as the carrier density increases. Similar features are observed from the hole side, but β turns out to be smaller than the electron side at same carrier density. Asymmetry also shows up in the prefactor α, which is 2~10 times larger on the hole side than the electron side. The result of the power law fitting is summarized in Table 4-1.

Table 4-1

Parameters extracted from power law fitting						
Carrier density ($\times10^{12}$ cm^{-2})	-2.8	-2.0	-1.0	1.0	2.0	2.8
ρ_0 (kohm)	0.752	0.631	0.797	0.700	0.495	0.487
α (kohm/K$^{\beta}$)	0.0120	0.00744	0.0115	0.00369	0.00305	0.00120
β	1.31	1.29	1.16	1.23	1.30	1.57

4.4.2 discussions and outlooks

The fitting to power law allows us to make a direct comparison to data in [58], where the measurement is also interpreted with the power law. Fig 4-10(a) summarizes the main conclusion that the power index follows a W-shape dependence on carrier density at small twist angle. The reduction of β is related to the modification of band structure near the van Hove singularities, manifested as small peaks near half-filling. Such a peak is in absence in our measurement, and β extracted from our measurement varies monotonically with carrier density. But considering the fitted β is in the similar range of ~1.2 to 1.6 as shown in Table 4-1, results are qualitatively in agreement except near half-filling.

In other works, the temperature dependence is analyzed with linear fit. Similar to what we find in Fig 4-13(b), the T-linear dependence is satisfied only in the intermediate temperature range, usually a few Kelvin to less than 100K for small twist angles (Fig 4-10(b), (c)). Theoretical works [64]indicates it might be determined by the underlaying mechanism that T-linear dependence is under domination only in the intermediate temperature range. On the contrary, the power law can be used to phenomenologically describe the temperature dependence, but it doesn't relate to any straight forward mechanism in theory. So, although the power law can fit data in a wider temperature range, it does not prove the failure of T-dependence interpretation but provides evidence that competing mechanism may exist in lower and higher temperature range. Besides, the power law relation can be expanded into terms accounting for contributions from competing mechanism. But such a theoretical treatment is beyond the scope of in this dissertation.

It is another interesting feature observed in our measurement that the local maximum at high carrier density shifts toward the CNP as the temperature increases. Similar feature is observed in other reported works [25, 62, 57] (Fig 4-1(a), Fig 4-17), but in short of detailed discussions. We find the

observed shifting in our data is of the most evident ones among all the data available. The shifting is strongly angle dependent, and is obvious in devices with twist angle of 1.24°[62]， 1.35°(device d151) and 1.50° (device d092, see next section), but is subtle in devices with twist angle of 1.8°~2° [25, 57, 58]. And careful measurement of the superlattice gap shows it has the double hump structure, making the scenario more complex (Fig 4-17(b)) [57]. Theoretical works to explain these features seem to be in absence.

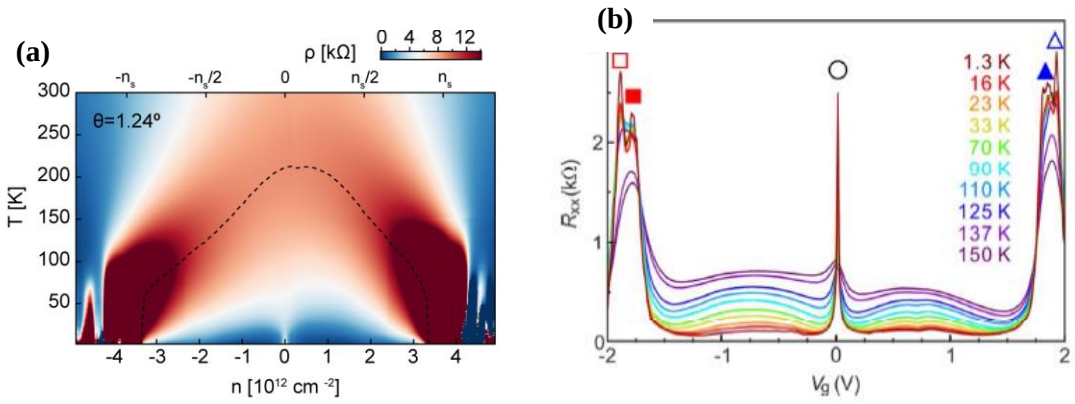

Fig 4-17 Features of the local maximum in resistivity (a) the shifting of maximum resistivity [62]. (b) the double hump structure of superlattice gap [57].

Asymmetry between the electron and hole side is observed throughout the transport measurement. In the case of graphene/hBN superlattice, umklapp electron-electron scattering dominates the resistivity in a wide range of temperature and carrier density, and results in a large excess resistivity and asymmetry in the system [65]. Measurement from our tBLG device indicates umklapp electron-electron scattering may also exist in tBLG superlattice. The feature of pronounced asymmetry between the electron and hole side makes umklapp scattering a promising candidacy to explain the temperature dependence of tBLG. Umklapp scattering has quadratic temperature dependence,

while the phenomenological power law fitting gives β ranging from ~1.2 to 1.6, depending on the carrier density, so umklapp scattering can't be the only source of excess resistivity. We hypothesize that it's a co-existing mechanism along with the phonon scattering proposed in [62].

The flat band introduced by the moiré patterns in 2D materials provide a new platform to study strong corelated systems. Novel experimental results keep being reported during the preparation of this dissertation. Evidence of the Ferromagnetism state is reported in twisted double bilayer graphene device recently [66]. In our collaborative work, corelated insulating and superconducting states are reported in a tBLG device with twist angle of 0.93° [67]. Related researches are still under debate in many aspects. Two examples are given here: the tBLG devices with small twist angle behave drastically different from AB stack bilayer. How the electronic properties of tBLG converge to AB stack bilayer graphene as the twist angle approaches zero is still a mystery. The Harper-Hofstadter bands of graphene subjected to a superlattice potential induced by aligned graphene/hBN heterostructures have been observed [68]. Similar effects are expected in tBLG superlattice [10] but haven't been reported yet. We will continue working on these topics to uncover the fascinating physics behind.

Chapter 5 Conclusions

In this dissertation, I reported our work on van der Waals heterostructure devices. Graphene based heterostructure devices show different properties as we vary the arrangement of carbon layers. From the aspect of transport experiments, a good understanding of the physics behind it requires efforts on fabrication, characterization, measurements and data analysis. The preparation of 2D materials using mechanical exfoliation method is introduced. And the procedures and recipes for device fabrication are recorded. We investigate several characterization methods: Raman spectroscopy, SEM and AFM. Raman spectroscopy is used to identify the number of layers of graphene flakes, and Raman spectrums of graphene on different substrates are compared. We also show Raman spectroscopy measurement of tBLG samples with twist angle of ~ 12°, and the enhancement of the G peak is observed. SEM and AFM are used to image defects in the stack. These imaging methods give us a guideline in improving the quality of devices. We verify the importance of the removal of tape and other polymer residuals for making defect-free devices. A polymer free monolayer graphene device with mobility of ~150,000 $cm^2 \cdot V^{-1} \cdot s^{-1}$ is reported and the

quantum Hall effect is observed. We also fabricated tBLG devices using the tear-and-stack strategy. The twist angle is calculated from the carrier density where the superlattice gap is induced. Here devices with twist angle of 1.35° and 1.50° are reported. Magnetoconductance measurements show Landau fans with filling factor of $\nu = 4, 8, 12, \ldots$ originate from the CNP and the superlattice gap. We observed evident asymmetry between the electron and hole side. We also observed resistive areas in Landau fan diagram at finite perpendicular magnetic field. Further theoretical work is needed to understand these observations. Temperature dependence measurements on tBLG sample show special features. The excess resistivity is fitted with power law dependence on temperature. We hypothesize there is a co-existing mechanism of phonon scattering and umklapp electron-electron scattering. Our observations provide information to help understand the correlated behaviors in tBLG.

Reference

1. Neto, AH Castro, et al. "The electronic properties of graphene." *Reviews of modern physics* 81.1 (2009): 109.

2. Wallace, Philip Richard. "The band theory of graphite." *Physical Review* 71.9 (1947): 622.

3. Cooper, Daniel R., et al. "Experimental review of graphene." *ISRN Condensed Matter Physics* 2012 (2012).

4. Novoselov, Kostya S., et al. "Two-dimensional gas of massless Dirac fermions in graphene." *Nature* 438.7065 (2005): 197.

5. Malard, L. M., et al. "Probing the electronic structure of bilayer graphene by Raman scattering." *Physical Review B* 76.20 (2007): 201401.

6. McCann, Edward, and Vladimir I. Fal'ko. "Landau-level degeneracy and quantum Hall effect in a graphite bilayer." *Physical Review Letters* 96.8 (2006): 086805.

7. Trambly de Laissardière, G., Didier Mayou, and Laurence Magaud. "Localization of Dirac electrons in rotated graphene bilayers." *Nano letters* 10.3 (2010): 804-808.

8. Bistritzer, Rafi, and Allan H. MacDonald. "Moiré bands in twisted double-layer graphene." *Proceedings of the National Academy of Sciences* 108.30 (2011): 12233-12237.

9. Dos Santos, JMB Lopes, N. M. R. Peres, and AH Castro Neto. "Graphene bilayer with a twist: electronic structure." *Physical review letters* 99.25 (2007): 256802.

10. Moon, Pilkyung, and Mikito Koshino. "Energy spectrum and quantum Hall effect in twisted bilayer graphene." *Physical Review B* 85.19 (2012): 195458.

11. Cao, Yuan, et al. "Correlated insulator behaviour at half-filling in magic-angle graphene superlattices." *Nature* 556.7699 (2018): 80.

12. Cao, Yuan, et al. "Unconventional superconductivity in magic-angle graphene superlattices." *Nature* 556.7699 (2018): 43.

13. Neil W. Ashcroft, N. David Mermin “Solid State Physics” *Cengage Learning* ***ISBN-10:*** *0030839939.*

14. Von Klitzing, Klaus. "The quantized Hall effects." *Reviews of Modern Physics* 58.3 (1986): 519.

15. Girvin, S. M., and R. Prange. "The quantum Hall effect." (1987): 401.

16. Gusynin, V. P., and S. G. Sharapov. "Unconventional integer quantum Hall effect in graphene." *Physical review letters* 95.14 (2005): 146801.

17. Novoselov, Kostya S., et al. "Unconventional quantum Hall effect and Berry’s phase of 2π in bilayer graphene." *Nature physics* 2.3 (2006): 177.

18. Zhang, Yuanbo, et al. "Experimental observation of the quantum Hall effect and Berry's phase in graphene." *nature*438.7065 (2005): 201.

19. Ebbesen, Thomas W., and Hidefumi Hiura. "Graphene in 3-dimensions: Towards graphite origami." *Advanced Materials* 7.6 (1995): 582-586.

20. Lu, Xuekun, et al. "Patterning of highly oriented pyrolytic graphite by oxygen plasma etching." *Applied Physics Letters*75.2 (1999): 193-195.

21. Novoselov, Kostya S., et al. "Electric field effect in atomically thin carbon films." *Science* 306.5696 (2004): 666-669.

22. Ferrari, Andrea C., et al. "Raman spectrum of graphene and graphene layers." *Physical review letters* 97.18 (2006): 187401.

23. Wang, L., et al. "One-dimensional electrical contact to a two-dimensional material." *Science* 342.6158 (2013): 614-617.

24. Geim, Andre K., and Irina V. Grigorieva. "Van der Waals heterostructures." *Nature* 499.7459 (2013): 419.

25. Cao, Y., et al. "Superlattice-induced insulating states and valley-protected orbits in twisted bilayer graphene." *Physical review letters* 117.11 (2016): 116804.

26. Kim, Kyounghwan, et al. "Tunable moiré bands and strong correlations in small-twist-angle bilayer graphene." *Proceedings of the National Academy of Sciences* 114.13 (2017): 3364-3369.

27. Ferrari, Andrea C., et al. "Raman spectrum of graphene and graphene layers." *Physical review letters* 97.18 (2006): 187401.

28. Ferrari, Andrea C., and Denis M. Basko. "Raman spectroscopy as a versatile tool for studying the properties of graphene." *Nature nanotechnology* 8.4 (2013): 235.

29. Ferrari, Andrea C. "Raman spectroscopy of graphene and graphite: disorder, electron–phonon coupling, doping and nonadiabatic effects." *Solid state communications* 143.1-2 (2007): 47-57.

30. You, YuMeng, et al. "Edge chirality determination of graphene by Raman spectroscopy." *Applied Physics Letters* 93.16 (2008): 163112.

31. Kalbac, Martin, et al. "The influence of strong electron and hole doping on the Raman intensity of chemical vapor-deposition graphene." *ACS Nano* 4.10 (2010): 6055-6063.

32. Lucchese, Márcia Maria, et al. "Quantifying ion-induced defects and Raman relaxation length in graphene." *Carbon* 48.5 (2010): 1592-1597.

33. Gokus, Tobias, et al. "Making graphene luminescent by oxygen plasma treatment." *ACS nano* 3.12 (2009): 3963-3968.

34. Malard, L. M., et al. "Raman spectroscopy in graphene." *Physics Reports* 473.5-6 (2009): 51-87.

35. Gupta, Awnish, et al. "Raman scattering from high-frequency phonons in supported n-graphene layer films." *Nano letters*6.12 (2006): 2667-2673.

36. Wang, Ying Ying, et al. "Raman studies of monolayer graphene: the substrate effect." *The Journal of Physical Chemistry C* 112.29 (2008): 10637-10640.

37. Cong, Chunxiao, et al. "Raman characterization of ABA-and ABC-stacked trilayer graphene." *ACS nano* 5.11 (2011): 8760-8768.

38. Lui, Chun Hung, et al. "Imaging stacking order in few-layer graphene." *Nano letters* 11.1 (2010): 164-169.

39. Ni, Zhen Hua, et al. "Uniaxial strain on graphene: Raman spectroscopy study and band-gap opening." *ACS nano* 2.11 (2008): 2301-2305.

40. Carozo, Victor, et al. "Raman signature of graphene superlattices." *Nano letters* 11.11 (2011): 4527-4534.

41. Poncharal, Philippe, et al. "Effect of rotational stacking faults on the Raman spectra of folded graphene." *Physical Review B* 79.19 (2009): 195417.

42. Kim, Kwanpyo, et al. "Raman spectroscopy study of rotated double-layer graphene: misorientation-angle dependence of electronic structure." *Physical review letters* 108.24 (2012): 246103.

43. Lu, Chun-Chieh, et al. "Twisting bilayer graphene superlattices." *ACS nano* 7.3 (2013): 2587-2594.

44. Chen, Xu-Dong, et al. "High-Precision Twist-Controlled Bilayer and Trilayer Graphene." *Advanced Materials* 28.13 (2016): 2563-2570.

45. Coh, Sinisa, et al. "Theory of the Raman spectrum of rotated double-layer graphene." *Physical Review B* 88.16 (2013): 165431.

46. Kim, Kyounghwan, et al. "van der Waals heterostructures with high accuracy rotational alignment." *Nano letters* 16.3 (2016): 1989-1995.

47. Zeng, Y., et al. "High quality magnetotransport in graphene using the edge-free Corbino geometry." *Preprint at https://arxiv. org/abs/1805.04904* (2018).

48. Woods, C. R., et al. "Commensurate–incommensurate transition in graphene on hexagonal boron nitride." *Nature physics* 10.6 (2014): 451.

49. Kerelsky, Alexander, et al. "Magic Angle Spectroscopy." *arXiv preprint arXiv:1812.08776* (2018).

50. Couto, Nuno JG, et al. "Random strain fluctuations as dominant disorder source for high-quality on-substrate graphene devices." *Physical Review X* 4.4 (2014): 041019.

51. Tan, Y-W., et al. "Measurement of scattering rate and minimum conductivity in graphene." *Physical review letters*99.24 (2007): 246803.

52. Naik, Mit H., and Manish Jain. "Ultraflatbands and Shear Solitons in Moiré Patterns of Twisted Bilayer Transition Metal Dichalcogenides." *Physical review letters* 121.26 (2018): 266401.

53. Jin, Chenhao, et al. "Observation of moiré excitons in WSe 2/WS 2 heterostructure superlattices." *Nature* (2019): 1.

54. Lei, Shiming, et al. "High mobility in a van der Waals layered antiferromagnetic metal." *arXiv preprint arXiv:1903.03111*(2019).

55. Lee, Dong Su, et al. "Quantum Hall effect in twisted bilayer graphene." *Physical review letters* 107.21 (2011): 216602

56. Schmidt, Hennrik, et al. "Superlattice structures in twisted bilayers of folded graphene." *Nature communications* 5 (2014): 5742.

57. Kim, Youngwook, et al. "Charge inversion and topological phase transition at a twist angle induced van Hove singularity of bilayer graphene." *Nano letters* 16.8 (2016): 5053-5059.

58. Chung, Ting-Fung, Yang Xu, and Yong P. Chen. "Transport measurements in twisted bilayer graphene: Electron-phonon coupling and Landau level crossing." *Physical Review B* 98.3 (2018): 035425.

59. dos Santos, JMB Lopes, N. M. R. Peres, and AH Castro Neto. "Continuum model of the twisted graphene bilayer." *Physical Review B* 86.15 (2012): 155449.

60. Fang, Shiang, and Efthimios Kaxiras. "Electronic structure theory of weakly interacting bilayers." *Physical Review B* 93.23 (2016): 235153.

61. Yankowitz, Matthew, et al. "Tuning superconductivity in twisted bilayer graphene." *Science* (2019): eaav1910.

62. Polshyn, Hryhoriy, et al. "Phonon scattering dominated electron transport in twisted bilayer graphene." *arXiv preprint arXiv:1902.00763* (2019).

63. Cao, Yuan, et al. "Strange metal in magic-angle graphene with near Planckian dissipation." *arXiv preprint arXiv:1901.03710* (2019).

64. Wu, Fengcheng, Euyheon Hwang, and Sankar Das Sarma. "Phonon-induced giant linear-in- T resistivity in magic angle twisted bilayer graphene: Ordinary strangeness." *arXiv preprint arXiv:1811.04920* (2018).

65. Wallbank, J. R., et al. "Excess resistivity in graphene superlattices caused by umklapp electron–electron scattering." *Nature Physics* 15.1 (2019): 32.

66. Liu, Xiaomeng, et al. "Spin-polarized Correlated Insulator and Superconductor in Twisted Double Bilayer Graphene." *arXiv preprint arXiv:1903.08130* (2019).

67. Codecido, Emilio, et al. "Correlated Insulating and Superconducting States in Twisted Bilayer Graphene Below the Magic Angle." *arXiv preprint arXiv:1902.05151* (2019).

68. Spanton, Eric M., et al. "Observation of fractional Chern insulators in a van der Waals heterostructure." *Science*360.6384 (2018): 62-66.